A UHF RFID System for Measuring dc Magnetic Field on HVdc Transmission Lines

by

Shijie Fu

A thesis submitted to the Faculty of Graduate Studies of
The University of Manitoba
in partial fulfillment of the requirements of the degree of

Master of Science

Department of Electrical and Computer Engineering
Price Faculty of Engineering
University of Manitoba
Winnipeg, MB, Canada

Examining Committee

This thesis was examined and approved by the following examining committee on December 13, 2024:

- **Prof. Behzad Kordi** (advisor)
  Department of Electrical & Computer Engineering
  University of Manitoba
- **Prof. Greg E. Bridges** (co-advisor)
  Department of Electrical & Computer Engineering
  University of Manitoba
- **Prof. Cyrus Shafai**
  Department of Electrical & Computer Engineering
  University of Manitoba
- **Dr. Miodrag Kandic**
  Department of Electrical & Computer Engineering
  University of Manitoba

Abstract

High-voltage direct current (HVdc) transmission lines are gaining more attention as an integral part of modern power system networks. Monitoring the dc current is important for metering and development of dynamic line rating control schemes. However, this has been a challenging task and there is a need for wireless sensing methods with high accuracy and dynamic range. Conventional methods require direct contact with the high-voltage conductors and utilize bulky and complex equipment. In this thesis, an ultra high frequency (UHF) radio frequency identification (RFID) based sensor is introduced for monitoring the dc current of an HVdc transmission line. The sensor is comprised of a passive RFID tag with a custom designed antenna, integrated with a Hall effect magnetic field device and an RF power harvesting unit. The dc current is measured by monitoring the dc magnetic field around the conductor using the Hall effect device. The internal memory of the RFID tag is encoded with the magnetic field data. The RFID tag enables remote wireless interrogation using a conventional RFID reader. The advantage of this approach is that the sensor does not require batteries and does not need additional maintenance during its lifetime. This is an important feature in a high voltage environment where any maintenance requires either an outage or special equipment.

In this thesis, the detailed design of the RFID tag is presented, including the antenna design and measurements for both the RFID tag and the RF harvesting section, the microcontroller interfacing design and testing, the magnetic field sensor calibration and the RF power harvesting section. The UHF RFID-based magnetic field sensor was fabricated and tested in a laboratory experimental setup.

In the experiment, a 40 mm diameter aluminum conductor, typically used in 500 kV HVdc transmission lines to carry dc current of up to 1200 A, is used to conduct dc current tests for the fabricated sensor. The sensor was attached to the conductor such that the Hall effect device was 30 mm from its surface. A dc current in the range of 100 – 1200 A was measured with an accuracy of better than 10% for a reader-to-sensor distance of 1 m.

Acknowledgements

I want to take this moment to express my appreciation to all those who have supported me throughout my two and half years of master's program.

First and foremost, my deepest appreciation goes to my advisors, Dr. Behzad Kordi and Dr. Greg Bridges, for their support and supervision throughout this research. Their guidance inspired me to overcome the challenges of my work, and their personal and academic support will continue to serve as a foundation for my future career and academic pursuits.

I would like to express many thanks to Daryl Hamelin, Oleg Shevchenko, and the University of Manitoba McMath High Voltage Lab, particularly for all their cooperation and guidance for test setup design and preparation. I also want to thank Emerich Kovacs III and David Stewart for all their practical consultations.

I would also like to acknowledge the financial support from Natural Sciences and Engineering Research Council of Canada (NSERC), Manitoba Hydro, Mitacs, and the University of Manitoba Faculty of Graduate Studies.

Thanks to all my course instructors, professors, and department staff for creating a fantastic learning experience. I am also grateful to my fellow students for their supports both academically and emotionally. I deeply appreciate all their valuable comments and guidance.

Many thanks to my thesis examining committee, Dr. Cyrus Shafai and Dr. Miodrag Kandic for their comments and suggestions to enhance this thesis.

Lastly, I deeply appreciate my parents and my partner, Wanting, for their kindness, patience, and support while I was pursuing my studies. Infinite thanks for their encouragement and for always being there for me. Their encouragement and trust made me successful in achieving my life goals. To all of my friends who have journeyed along with me and witnessed my growth during my treasurable time in Canada, the experience and support I received are greatly appreciated.

The final thanks to myself for all the hard work and never giving up.

Table of Contents

List of Figures

List of Tables

Nomenclature

ASK	Amplitude Shift Keying
BAP	Battery Assisted Passive
CPS	Coplanar Stripline
DCCT	Direct Current Current Transformer
GMR	Giant Magnetoresisitance
HVdc	High Voltage direct current
RF	Radio Frequency
RFID	Radio Frequency Identification
RFIC	Radio Frequency Integrated Circuit
RSS	Received Signal Strength
VNA	Vector Network Analyzer

Chapter 1

Introduction

1.1 Motivation

Overhead high-voltage direct current (HVdc) transmission lines are gaining increased attention as an integral part of modern power system networks. The demand for HVdc power transmission has grown rapidly with the rising integration of renewable energy sources, long-distance power transport, and increased interconnection of power grids across territories and countries [1]. HVdc technology is advantageous for long-distance transmission due to its ability to reduce transmission losses, improve stability, and efficiently transport high-power loads [2]. An HVdc conductor that carries a high dc current generate a strong magnetic field along the transmission line, which pose a challenge to the monitoring and maintenance processes that ensure HVdc transmission network remain stable, reliable, and safe. Moreover, the magnetic field generated by an HVdc conductor can be used as a reliable, non-invasive indicator of the current flowing through the conductor. Measuring magnetic field makes non-contact measurement of HVdc current possible which improves safety and

reduces maintenance complexities [3–5]. This rises the need of an advanced sensing technology that is capable of measuring magnetic fields and monitoring current which are essential for the effective operation of HVdc infrastructure.

Conventional magnetic field sensors are often adopted from alternating current (ac) systems, typically need an external power source, complex installation, and maintenance. In ac systems, the alternating magnetic field generated by the conductor can be coupled with coils to harvest energy for powering sensors or measuring the generated magnetic field, according to Faraday's law of induction. However, that is not possible in HVdc transmission lines since the field is static. The magnetic field generated by HVdc transmission lines are usually stronger and more consistent. The direct current current transformer (DCCT) is the most accurate dc high current measurement sensor that is commercially available [6]. The calibration and installation of a DCCT are challenging and complex [7, 8]. A DCCT generates a magnetic field in the opposite direction to cancel out the magnetic field generated by the HVdc transmission line for measurement purposes. These sensors are usually bulky and require direct contact with the line which requires proper insulation and regular maintenance. Additionally, an external power source is needed, as the sensor cannot harvest energy from ambient sources. After the measurement phase, an information transmission system is needed to acquire the data, and this process is typically not wireless. As HVdc transmission expands, the limitations of existing sensors in detecting and interpreting magnetic fields around HVdc lines highlight the need for reliable and wireless solutions that can meet the unique demands of this growing infrastructure.

Radio frequency identification (RFID) technology is a promising and well developed wireless communication method [9]. RFID technology is widely used in different places, such as inventory management, asset tracking, and supply chain management because of

its simplicity, efficiency, and the ability to communicate wirelessly over short to medium ranges. RFID tags are mostly passive, i.e. they do not require an internal source of power. They get enough power directly from the RFID reader's incident wave to power up the integrated circuit. RFID tags can be designed with integrated sensors to measure different parameters [10]. By incorporating an RFID tag with a microcontroller and a sensor, the sensor's data can be processed and transmitted by the RFID tag's chip. RFID tags can accommodate various sensor types by integrating an RF energy harvesting section on the tag, providing sufficient power for the sensor and microcontroller. For example, in this work, an RFID tag equipped with a magnetic field sensor can utilize this harvested energy to measure the magnetic field and wirelessly transmit the data back to the reader. This transmission is typically accomplished within a few milliseconds. This passive power mechanism makes RFID ideal for wireless sensing applications on lines within converter stations, or along the DC line between the stations where replacing batteries or maintenance is challenging. The adaptability of RFID technology allows it to be used not only for data transmission but also for sensing applications in power systems, such as magnetic field monitoring and current measurement on overhead transmission lines.

1.2 Research Objectives

The objective of this research is to design, fabricate, and test a UHF RFID system for measuring DC magnetic fields on HVdc transmission lines. The fabricated sensor is designed to measure magnetic field within a dynamic range of 4.5 mT, which is the typical magnetic field near the surface of conductors used in HVdc transmission lines. The design phase of this work includes developing the RFID antenna, RF power-harvesting antenna, microcontroller

interfacing, RF power harvester integration with the RFIC, and overall system assembly. The system is required to follow the UHF Gen 2 Air Interface Protocol, established by EPCglobal and standardized as ISO 18000-6C. This protocol specifies communication standards for UHF RFID systems, detailing how data is encoded, modulated, and how anti-collision protocols are managed, ensuring accurate and efficient RFID communication [11]. The first objective is to design both the RFID tag antenna and the power-harvesting antenna for the UHF RFID tag. To achieve maximum efficiency, it is essential to ensure the a good impedance match exists between the RFID antenna and the RFIC. This optimization helps achieve the objective of ensuring a minimum reading range of 1 meter. The power-harvesting antenna should have a gain of no less than 0 dBi. The second objective is to interface a commercial magnetic field sensor with a microcontroller, which will be programmed to write the measured magnetic field data into the RFIC's memory. Additionally, an RF power harvester must be integrated with the RFID tag to supply adequate power for measuring the magnetic field.

The fabricated system was tested on an HVdc conductor that carries a current of maximum 1.2 kA which is the maximum current of the dc source introduced in Appendix C. The fabricated system was placed 3 cm away from the conductor. During data acquisition, the system measured the magnetic field strength and transmit these data to an RFID reader, with minimal interference from the surrounding wireless devices. These results will be compared with simulation solutions calculated using a commerical finite element software (COMSOL Multiphysics) and used to validate the ability of the fabricated system to withstand high magnetic fields and confirm its functional reliability and accuracy under real-world conditions.

1.3 Contributions

The contributions of this thesis are as follows:

- Design of an RFID tag integrated with a microcontroller and an RF power harvester. This includes two antenna designs for both the RFID tag and RF harvester, a PCB layout design and fabrication.
- Design of a software platform that converts an analog voltage from the Hall effect sensor into digital value and interfaces a PIC microcontroller to transmit the magnetic field sensor to the radio frequency integrated circuit using serial peripheral interfacing (SPI).
- Conduct experiments to verify the operation of the system. The measured sensitivity is 27.1 mV/mT, with maximum 10% deviation and measurement resolution of the designed UHF RFID system is ±90 A. The maximum reading range is 2 m.

1.3.1 Publications

The outcome of this study has been published as follows:

1. S. Fu, G. E. Bridges, B. Kordi, "Application of Radio Frequency Identification (RFID) in Power Systems Monitoring" in *CIGRE Canada 2024*, Winnipeg, Canada, 28-31 Oct. 2024 [12].

   The application of RFID sensing system in power system and the potential of RFID sensing system were presented in this paper

2. S. Fu, G. E. Bridges, and B. Kordi, "Magnetic field monitoring on HVdc transmission lines using a UHF-RFID tag," in 2024 *Photonics and Electromagnetics Research Symposium* (PIERS 2024), Chengdu, China, 21-25 April 2024 [13].

   This paper won Second place in Best Student Paper Competition, The proof of concept for the idea of using an RFID-based sensing system for measuring the magnetic field around HVDC conductors was presented.

3. S. Fu, G. E. Bridges, and B. Kordi, "RFID Sensor with Integrated Energy Harvesting for Wireless Measurement of dc Magnetic Fields," *MDPI Sensors*, in preparation.

   The fabricated RFID based magnetic field sensor will be introduced in this journal paper.

1.4 Thesis Outline

This thesis is organized into seven chapters as defined below:

Chapter 1: Motivation, research objectives, and contributions are presented.

Chapter 2: Different types of magnetic field sensor were discussed. Each kind of sensor was explained in detail regarding its working principle and suitability in application in overhead transmission line monitoring. Hall effect sensor and magnetoreisitive sensor are two candiates for the final decision of magnetic field sensor selection in this thesis. In Chapter 4, both sensors are examined and tested in the laboratory. Moreover, an introduction to RFID technology was given, including the RFIC schematic, modulation techniques. EM4325 RFIC is used to build the RFID based magnetic field sensor in this thesis. Lastly, sensors based on RFID technology for different parameters were presented, and the existing topic of RFID based sensor in power system monitoring was presented.

Chapter 3: Both the RFID antenna and RF power harvester antenna design was presented. The design approach and the procedure were explained in details. The dimensions of both antennas were presented. Both antennas were fabricated on an FR4 substrate with a thickness of 0.6 mm and relative permittivity of 4.4. Both antennas were tested using half antenna testing method to find out the actual antenna's input impedance. The antenna gain of the power harvester antenna is measured using a relative antenna gain method. The gain measured is around 1 dBi. The next chapter covers the selection of magnetic field sensor and the detailed testing method to evaluate the performance of different magnetic field sensors.

Chapter 4: two different types of commercial magnetic field sensors are tested using a solenoid to generate a wide range of magnetic fields. The Hall effect sensor demonstrates high accuracy and a wide linear range for measuring magnetic fields. It is capable of measuring fields up to 14 mT with a sensitivity of 100 mV/mT. The magnetoresistive sensor, while highly sensitive, has a linear range of only up to 0.6 mT, which is much lower than the magnetic field levels around HVdc lines. After comparing the characteristics of the two sensor types, the Hall effect sensor is chosen for the implementation of the RFID-based magnetic field sensor.

Chapter 5: In this chapter, the power transmitter (RFID reader) used in this thesis is tested. A commercial UHF RFID tag is used to evaluate the reading range and received signal strength of the RFID reader. A wideband antenna measures the power level and frequency band of the transmitted wave. Details of the RF power harvester P2110B used in this thesis are provided, and its output waveform is measured using an oscilloscope. A cold-start charging time of 24.5 s and a recharging time of 5 s are achieved. The timeline of the measurement operation is shown.

Chapter 6: In this chapter, the high DC current setup for testing a Hall effect sensor and the fabricated sensor is presented. The first test validates the capability of using a Hall effect sensor to measure the magnetic flux density generated by a large DC current passing through an HVdc conductor. The second test evaluates the performance of the fabricated sensor. The sensor is tested at different sensor-conductor distances and reader-sensor distances. The results are compared with simulated results from a COMSOL Multiphysics simulation. The sensor demonstrates good performance in measuring the magnetic field around HVdc transmission lines, with a sensitivity of 27.1 mV/mT and a minimum current resolution of 90 A.

Chapter 7: Conclusions of this thesis project and potential future research work are discussed.

Chapter 2

Background

2.1 Magnetic Field Sensing

In modern power systems, high voltage overhead transmission lines and underground cables are essential for transporting electrical energy over long distances from generation stations to local distribution centers [14]. As power systems expand to meet the increasing demand from both domestic and industrial needs, monitoring high-voltage transmission lines has become a critical aspect of power system asset management. Magnetic field sensors are extensively used to monitor various parameters of overhead HVdc transmission lines, including current, voltage [15], sagging, galloping [16] and fault location detection [17]. Magnetic field measurements can be used to monitor overhead HVdc transmission lines. However, this task is inherently challenging, requiring the development of wireless sensing techniques that offer high accuracy and a wide dynamic range.

2.1.1 Hall Effect Sensor

In power systems, different types of sensors are employed to monitor magnetic fields, facilitating equipment monitoring and system optimization. Common types include Hall effect sensors, which provide reliable measurements in both static and dynamic fields, known for its high precision in detecting weak magnetic fields [18]. Other types, such as magnetoresistive and inductive sensors, offer unique characteristics like high sensitivity and compact size [19].

The Hall effect sensor is widely used for magnetic field measurement. It operates based on the Hall effect, a phenomenon discovered by Edwin Hall in 1879 [20]. This phenomenon occurs when a conducting plate is placed in a magnetic field normal to its surface, the magnetic field induces a force on the moving charges within the plate. This force causes the charges to accumulate on one side of the plate, creating a small voltage difference across it, as illustrated in Fig. 2.1. For commercial Hall effect sensors, manufacturers calibrate the device by mapping the Hall voltage to known magnetic field values.

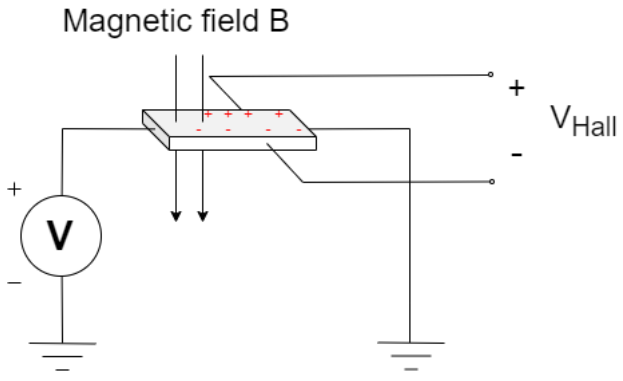

Fig. 2.1: Schematic of a Hall effect sensor showing the induced voltage due to a dc magnetic field.

2.1.2 Magnetoresistive Magnetic Field Sensor

Another type of magnetic field sensors used for measuring small magnetic fields that require better sensitivity is the magnetoresistive sensor. In 1990, large amount of giant magnetoresisitance (GMR) devices were massively developed for magnetic field sensing [19]. Magnetoresistive sensors operate based on the principle of giant magnetoresistance (GMR), resulting in a change in electrical resistance in response to an external magnetic field. When this material is in a magnetic field, the alignment of the magnetic domains within the sensor material changes. This alignment affects the ease with which electrons flow through the material, leading to a change in electrical resistance [19]. Since changes in resistance are not convenient to measure and transmit directly, the magnetoresistive sensor which normally consists of four GMRs will be used to form a bridge circuit as shown in Fig. 2.2. When there is no magnetic field across the sensitive axis, the resistance of all four resistors are identical and the output voltage will be zero. When exposed to a static magnetic field, the resistance of the top two resistors increases, while the resistance of the bottom two decreases by the same amount. The unbalance resistances will result in a voltage difference across the bridge. The voltage can be used to calculate the corresponding magnetic field base on the data-sheet provided by manufacturers.

2.1.3 Magnetic Fluid Magnetic Field Sensor

Magnetic fluid is a material which has an optical characteristic under magnetic field. Magnetic fluids (MF) possess a range of unique magneto-optical properties, such as adjustable refractive index (RI), the Faraday effect, linear dichroism, and linear birefringence, making them highly versatile for various optical applications [22, 23]. This unique behavior enables the fluid to act as a highly sensitive magnetic field sensor. A magnetic fluid magnetic field

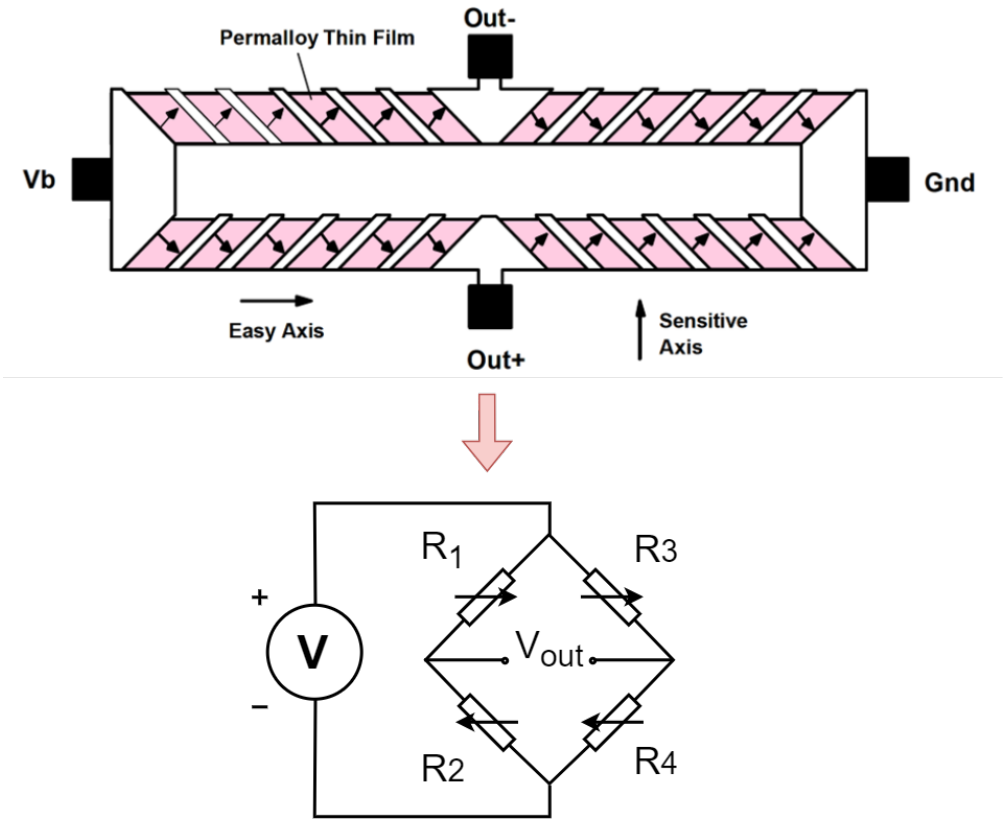

Fig. 2.2: Schematic of a Magnetoresistive sensor with its equivalent circuit diagram, the output of the circuit indicates the magneitc field intensity along the sensitive axis (top figure is adopted from [21]).

sensor consists of tiny magnetic nanoparticles suspended in a liquid carrier. When exposed to a magnetic field, the magnetic nanoparticles within the fluid align along the field lines. A laser beam is injected through the magnetic fluid and the intensity, phase and angle of the beam will change according to the change in RI. By monitoring changes in optical properties, the sensor provides a quantitative measurement of the magnetic field strength. The sensitivity of magnetic fluid based sensor can be adjust by changing the concentration of the magnetic nanoparticles. In [22], the concentration of the nanoparticles is 1.1 % which also has a maximum of 6 mT. The maximum magnetic field sensing intensity sensitivity of

-1.21268 dB/mT is obtained at the wavelength around 1580 nm. This sensor has also shown potential for applications in high-voltage transmission sensing [24]. However, the size of the sensor is large and requires a large optic measurement device and well-trained personnel.

2.1.4 Acoustic Magnetic Field Sensor

An acoustic magnetic field sensor is a type of passive wireless sensor. The sensor is equipped with an integrated RF rectifier to power the sensor. The sensor will convert the received RF power to a surface acoustic wave through the piezoelectric effect. The surface acoustic wave is used to couple with the magnetic field [25]. Similar to the sensor described in Section 2.1.2, this type of sensor has a giant magnetoresistive layer. The sensor uses the attenuation of the reflected surface acoustic wave from the giant magnetoresistive layer to calculate the intensity of the magnetic field. In [26], the author achieves a sensitivity of 1.18 dB/mT with a resolution of 0.1 mT. This highly integrated surface acoustic wave sensor demonstrates potentials for magnetic field measurement in high voltage transmission sensing. However, a barrier to mass production is the limited availability of suitable substrate material [27].

2.2 Radio Frequency Identification Technology

2.2.1 Fundamentals of RFID

Radio frequency identification (RFID) technology is a promising and well developed wireless communication method [9, 28]. Over the decades, the technology has seen rapid growth and widespread adoption in areas such as inventory management, transportation, access control, and asset tracking, where its ability to uniquely identify and communicate with tagged objects has been transformative [29].

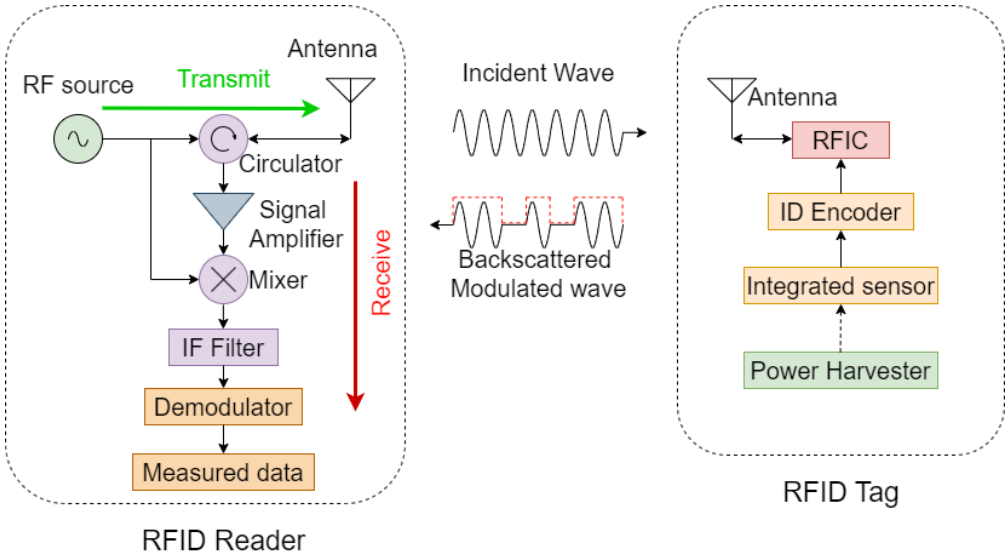

Fig. 2.3: Block diagram of a typical RFID system: An RFID reader and RFID tags. RFID tags might not be completely passive; a power harvester may be present.

Modern RFID systems offer user-accessible memory, which provides space to store data such as unique identification codes, timestamps, or sensor measurements. This feature enables RFID tags to be used in a wide array of applications that require both identification and data storage. Because RFID sensors can operate with extremely low power density, they can be detected from long distances with minimal energy requirements, making them suitable for applications where long-range detection is necessary.

An RFID system shown in Fig. 2.3 typically consists of two main components: an RFID reader and RFID tags [30]. The reader transmits an incident wave to the tag. The tag powers up and transmits back a backscattered, modulated wave that contains an ID code and sensor information from the tag. The key point of a passive tag is to acquire necessary power from the reader. In Fig.2.3 the signal path is labeled with green and red to transmit and receive RF signals. The detail of RFID reader will be discussed in Section 5.1.

RFID systems generally operate in three main frequency bands: high frequency (13.56 MHz), ultra-high frequency (902-928 MHz in North America, 865-868 MHz in Europe), and ultra-wideband (300-3000 MHz). Each frequency band is suited to different applications. High-frequency RFID systems can penetrate most materials, but they offer a short read range, lower data transfer rates, and typically support reading only one tag at a time. In contrast, ultra-high frequency and ultra-wide frequency band of RFID systems provide a long read range, high data transfer rates, and can read multiple tags simultaneously, though their performance can degrade when objects obstruct the RF wave path [31]. The selection of the appropriate frequency band depends on the specific requirements of the application. As shown in Fig. 2.4, when making payment using a credit card, near field communication is (NFC) used, it falls in to the high frequency band of RFID. Industry rely on RFID tags for asset management and warehouse tracking. UHF RFID are widely used in luggage tags nowadays, and the tag is capable of storing passenger information to prevent error during luggage drop off process.

2.2.2 UHF RFIC

A radio frequency integrated circuit (RFIC) is designed to operate at high frequencies, typically ranging from several hundred MHz to several GHz. This thesis focuses on the Ultra High Frequency (UHF) band, specifically the 902 MHz to 928 MHz range, which follows standard in North America for UHF RFICs [32]. The primary objective of an RFIC in an RFID tag is to facilitate reliable communication between the RFID reader and the tag, ensuring readability and a long working distance. An RFIC typically integrates various components, including amplifiers, filters, mixers, oscillators, modulators, and demodulators, onto a single chip (see in Fig. 2.5). It is directly connected to an antenna for transmitting and

Fig. 2.4: Some examples of RFID applications that operate in different frequency bands in our daily life.

receiving radio frequency signals. Filters are essential in an RFIC design, as the signals picked up by the antenna may not always be at the desired frequency. Bandpass filters are commonly used to isolate UHF band signals [9]. Low noise amplifiers (LNAs) amplify weak signals while filtering out noise. The modulator is used for signal modulation. Signal modulation in RFICs typically employs amplitude modulation (AM), with various modulation techniques discussed later in Section 2.2.3. The demodulator extracts the original information-carrying signal on the receiver side, determining whether to write a new code in the RFID tag or to read the existing code. An RF switch may also be included in the RFIC, directing high-frequency signals along the correct paths for receiving and transmitting. To maximize power efficiency, a matching network may be implemented. However, this is not always necessary, as the matching can often be achieved by designing the antenna to have an impedance that is the complex conjugate of the RFIC's input impedance.

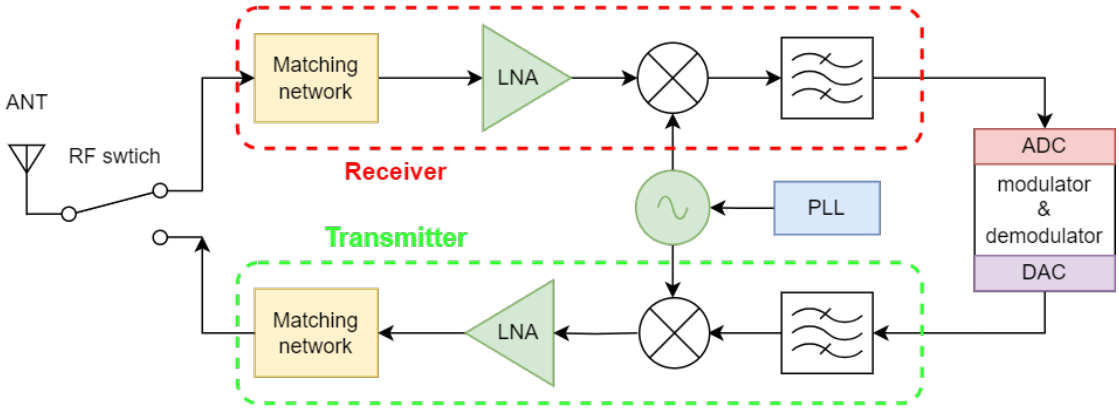

Fig. 2.5: Block diagram of a typical RFIC showing how signal is received and transmitted back to the RFID reader.

2.2.3 Modulation Techniques

Amplitude shift keying (ASK) is commonly used for signal modulation in RFID systems. In this technique, varying amplitudes of the signal represent a bit stream containing the encoded information, where a high amplitude could corresponds to a binary 1 and a low amplitude represents a binary 0 as shown in Fig. 2.6.

The receiver in the interrogation system identifies the bit stream by monitoring the voltage levels and determining if they exceed a predefined threshold voltage. The ratio of the threshold voltage to the signal voltage that indicates a binary 1 is called the modulation index. Ideally, the modulation index is 1 for the best signal-to-noise ratio. The ASK technique introduced above is a NRZ code which is commonly used in RFID systems. This method is efficient when number of 1s is equal to or greater than the number of 0s. This is to ensure that the tag receives consistent power that maintain its operation during the communication process. Another coding process in RFID systems is Manchester coding or bi-phase coding [33]. In Manchester coding, a binary 1 is represented by a negative transition in the

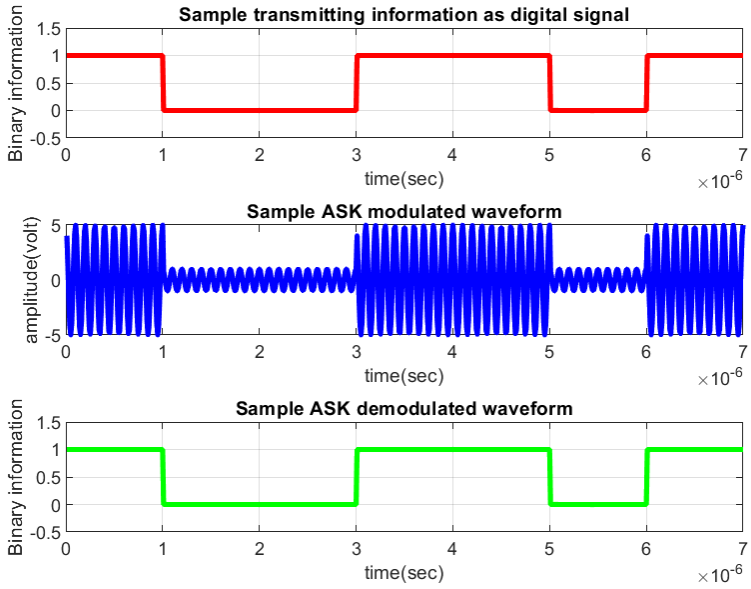

Fig. 2.6: Sample of modulation and demodulation using ASK.

middle of the bit period, while a binary 0 is represented by a positive transition. Due to this structure, Manchester coding is also known as split-phase coding [33].

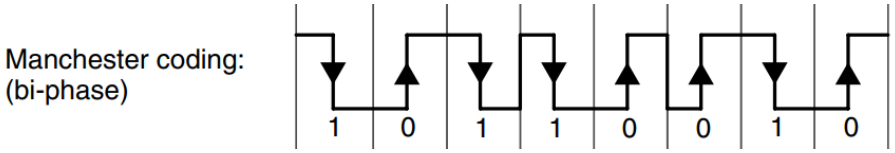

Fig. 2.7: Sample of Manchester coding process [33].

2.2.4 EM4325 RFIC

In this thesis, EM4325 RFIC is used for the RFID tag design. EM4325 is a highly integrated RFIC designed for use in a wide range of applications, including supply chain management, inventory tracking, and access control. This chip operates in the UHF frequency range (902-

928 MHz). Its compact size and low power consumption enable long read distances and fast data transmission rates. In addition, this chip is not only equipped with user-accessible memory but also supports advanced applications by providing programmable external interfaces and a 4-bit I/O port [34]. This means that the RFIC can be configured as an SPI master or slave to function as an RF front end and protocol handler in advanced RFID tags or embedded applications. The interfacing of the EM4325 chip is discussed in detail in Appendix A. By interfacing the chip with a microcontroller, the tag can be written through the reader or by a SPI master.

The battery-assisted passive (BAP) configuration is also a unique characteristic of EM4325 RFIC. In a BAP configuration, the EM4325 offers longer reading range. The reading range is determined by the reading sensitivity of the integrated circuit EM4325, which is $-8.3\,\mathrm{dBm}$. In BAP mode, the reading sensitivity is $-31\,\mathrm{dBm}$, which significantly increases the reading range. To enable BAP mode, the tag needs an additional power management circuit on the tag. The detailed power management module will be discussed in detail in Chapter 5.

2.2.5 RFID Integrated Sensor

An RFID-integrated sensor combines RFID technology with various types of sensors to enable wireless monitoring and data collection of environmental, mechanical,or electrical parameters [10, 35–38]. In this setup, sensors are integrated into an RFID tag, which allows the RFID based sensor to transmit not only unique identification information but also measurements. As shown in Fig. 2.8, an RFID-based sensor typically consists of an antenna, a microcontroller, a sensor, a power harvester, and a power storage and management circuit. The antenna is used to receive the incident wave from the RFID reader shown in Fig. 2.3 and transmit the backscattered modulated wave. A microntroller is used as a connector between

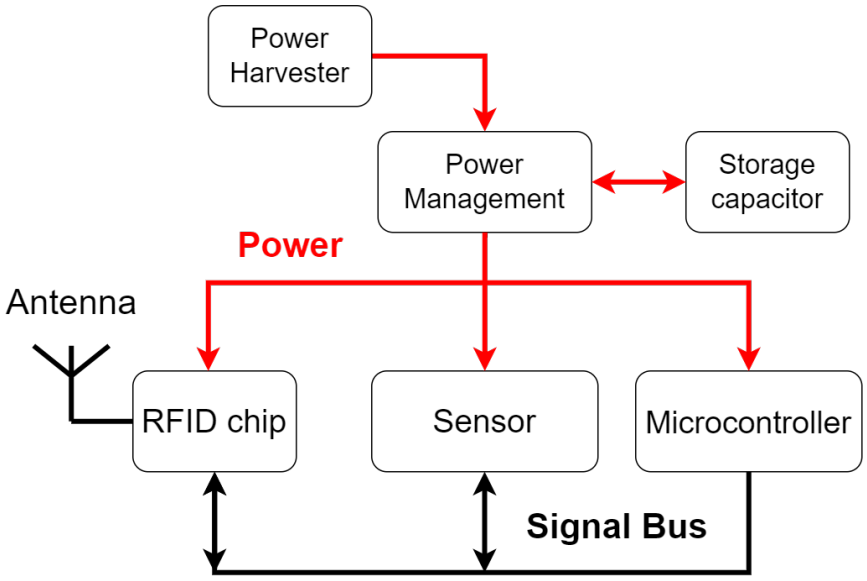

Fig. 2.8: Block diagram of a typical RFID sensing system. A power bus used to power up the entire circuit and a signal bus is used to write information to a passive RFIC.

a sensor and an RFIC. The output of a sensor is usually an analog signal and the microcontroller can convert it to a digital signal and then transmit it to the RFIC through different interfacing techniques. Power harvester is optional in a RFID based sensor, if the sensor gets enough power from the incident wave from the RFID reader. Normally the incident power is not enough to operate a microcontroller and a sensor. In this case, a power harvester and power management is essential. The power harvested will be stored in an energy storage component like a supercapacitor. The power management circuit will monitor the power level of the capacitor and turn on the output when it's fully charged. The power harvester is not limited to one kind of ambient source. Usually a rectenna will be employed with the power harvester to collect energy in different frequency bands [39–41]. In this thesis, the power harvester uses RF power from the incident wave and stores it in a supercapacitor.

The power harvester has its own antenna for harvesting power only and it's not responsible for the RFID reading part.

2.2.6 RFID Applications in Power System

RFID technology has been recognized as increasingly valuable technology in power system monitoring. It offers good solutions for asset management, equipment monitoring, and real-time data collection, which are critical for enhancing the reliability, efficiency, and safety of power infrastructure.

In [42–44], the authors presented a method that utilizes multiple UHF RFID-based sensors to wirelessly collect vibration signals from various points within a power transformer to identify fault locations. As discussed in Section 2.2.5, this RFID vibration sensor required more power to operate the circuit in the tag. The RFID sensor tag uses an inductive solenoid by coupling with the transformer's ambient AC magnetic field of the transformer to power the tag. The maximum power consumption of the RFID sensor tag is 147 μW and the power harvester can provide 197 μW extracted from a 50 Hz magnetic field. In [45], a chipless RFID sensor is used to measure the time-varying electric field in a HVac assets. The sensor comprises an RF resonator equipped with back-to-back varactor diodes. When AC electric field is present, the voltage induced across the varactor diode will change the resonant frequency of the RF resonator. The change of resonant frequency is used to map to a corresponding electric field intensity. Similarly, in [46–48], the authors introduced the concept of using a PD sensing coil together with a Schottky diode and chipless RFID tag to detect PD events inside a power transformer. A PD sensing coil is used to collect the UHF signal generated by PD events inside the transformer. The coil will induce a voltage across a Schottky diode. When the diode is forward biased, the resonance frequency of the tag will

change. No study has been done on the magnetic field and current measurement using an RFID based sensor for overhead transmission line monitoring.

2.3 Summary

In Chapter 2, different types of magnetic field sensor were discussed. Each kind of sensor was explained in detail regarding its working principle and suitability in application in overhead transmission line monitoring. Hall effect sensor and magnetoreisitive sensor are two candiates for the final decision of magnetic field sensor selection in this thesis. In Chapter 4, both sensors are examined and tested in the laboratory. Moreover, an introduction to RFID technology was given, including the RFIC schematic, and modulation techniques. EM4325 RFIC is used to build the RFID based magnetic field sensor in this thesis. Lastly, sensors based on RFID technology for different parameters were presented, and the existing topic of RFID based sensor in power system monitoring was presented as well. The next chapter contains an introduction to RFID readers and a performance evaluation of the RFID reader used in this thesis.

Chapter 3

Design and evaluation of RFID and power harvester antenna

3.1 RFID Antennas

The design and performance of antennas are fundamental for effective wireless communication. In RFID systems, the antenna is the most important part in determining the range, power efficiency, and reliability of wireless information transfer. This chapter presents the common antenna matching techniques and the detail design of both RFID tag antenna and power harvesting antenna, and their performance evaluation.

3.1.1 Matching Technique

To optimize power transfer and transmission range for an RFID tag, the tag antenna's input impedance is matched to the complex conjugate of the RFIC's input impedance as this would maximize the efficiency of the RFID tag. Since most of the RFIC are not internally matched

to 50 Ω, it is essential to design the tag antenna's impedance to be matched to the RFIC impedance. As discussed in Section 2.2.2, RFIC normally has a large capacitive part. So a normal planar dipole antenna which is mainly resistive and less reactive, is not suitable in this case. In the following sections, a few matching techniques will be presented.

T-Match Method

The T-Match method is one of the most popular impedance matching technique for UHF RFID tags [49]. This is a simple and adaptable design with not much increase in size and cost. The stub introduced at the center of the antenna increases the reactive part of the antenna's impedance. As shown in Fig. 3.1, the design is simple, but not much design flexibility is available. T-match antennas are generally effective for narrowband applications. While the matching network can be fine-tuned for a particular frequency, its performance may degrade significantly outside that frequency range. As a result, it may not be the best choice for applications that require wider bandwidth or need to operate at multiple frequencies. When designing a T match antenna for a particular frequency, the size of the overall antenna is fixed. To fit the antenna to a small RFID tag format, the only solution is to use high dielectric materials.

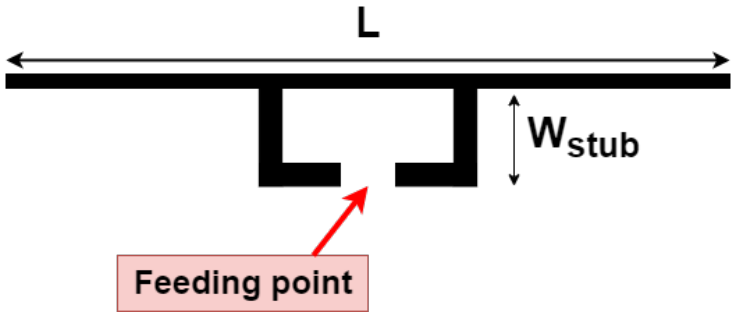

Fig. 3.1: T-match antenna for matching a RFID tag to the input impedance of an RFIC [49].

Coplanar Stripline Matching

A coplanar stripline antenna is a type of antenna design that utilizes a coplanar stripline transmission structured for radiation. The coplanar stripline structure provides an effective solution by enabling easy integration with RFICs and by maintaining controlled impedance for efficient matching. It is easy to tune both real and imaginary part of the input impedance of the antenna. The coplanar configuration offers considerable design flexibility [50]. By changing the geometry (i.e. L_s, the length of the stripline, W_s, the width of the stripline, L, the overall antenna length), the input impedance of the antenna can be fine tuned for matching. Coplanar stripline antennas also have a narrow bandwidth compared to other types of antennas, such as patch antennas. The narrow bandwidth makes it suitable for application in UHF RFID tag design since the frequency band in North America is quite narrow.

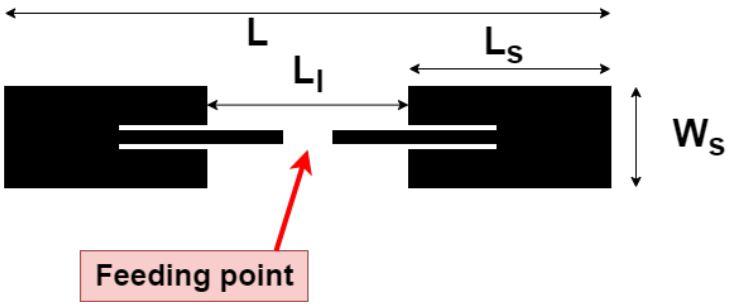

Fig. 3.2: Coplanar stripline antenna for matching a RFID tag to the input impedance of an RFIC [50].

Inductive Feeding Loop Matching

An inductively coupled feed antenna has two main components: the feed loop and the antenna, which is usually a dipole. Instead of a direct electrical feed to the dipole antenna,

a loop is added to inductively couple with the dipole. This method is applied in antenna design when a low resistive component and a high reactive component are required. When the RF signal excites the dipole antenna to radiate, it generates a magnetic field around the antenna. This magnetic field then induces a current in the loop due to its proximity to the dipole antenna. For designing the antenna with an inductive feeding loop, there is not much flexibility on the dipole size as it has to be designed for a specific frequency band. The size of the loop and the distance between the loop and the dipole control the mutual impedance between the loop and the dipole. This will allow matching the antenna to an RFIC.

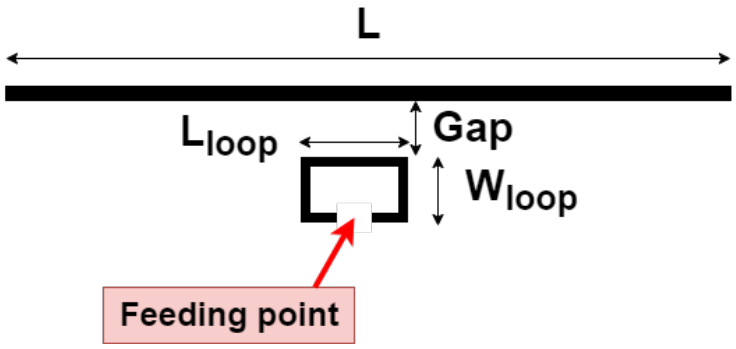

Fig. 3.3: Dipole antenna with an inductive feeding loop for matching a UHF RFID tag [51].

3.2 UHF RFID Antenna Design

As discussed in Section 3.1, a key component in designing an efficient RFID tag is its antenna. A well-matched antenna design is essential for optimizing both the read range and the communication efficiency of the sensor tag. The RFID chip EM4325 has an input impedance of $Z_{\text{in}} = 7.6 - j114\,\Omega$ at 915MHz when operating in BAP mode [34]. The RFID tag antenna needs to be designed to match the input impedance of the RFIC to maximize the efficiency. The antenna was designed and simulated using Ansys HFSS. The simulation is conducted

using a 0.6 mm FR4 dielectric. In this thesis, a coplanar stripline (CPS) antenna [52, 53] is employed as a suitable choice for this purpose. Using a CPS antenna is not the first option at the beginning of the RFID antenna design, since it's hard to determine a correct size such that the input impedance of the antenna matches to the RFIC in the first design. The CPS antenna used in this thesis follows the design path shown in Fig 3.4. All antennas in this design path is simulated using Ansys HFSS to find out the input impedance of the antenna design. The antenna design started with a planar dipole antenna that resonates at 915 MHz. Since most substrate used for building an RFID antenna are thin and have a low dielectric constant, the free-space assumption can be applied when designing antennas. The dipole antenna is designed to have a length of 0.47λ [54]. The wavelength λ is calculate using

$$\lambda = \frac{c}{f} = 0.3278 \text{ m} \tag{3.1}$$

where c is the speed of light and f is the operating frequency, in this case 915 MHz. The resulted overall dipole length is 15.4 cm. In this configuration, the imaginary part is nearly zero. To reduce the real part of the antenna impedance, two coplanar striplines were added at the ends of the antenna. The overall size of the antenna, as well as the real part of the impedance, decreased significantly from 65.82 Ω to 22.91 Ω. However, the imaginary part of the antenna's impedance became capacitive, which is not ideal for matching the RFIC. The next step was to introduce a large inductive component to the antenna impedance. By adding a coupled loop near the planar dipole, a significant inductive component is introduced to the antenna [51,55]. The final CPS configuration wiht a inductive loop feeding method effectively matches the antenna to the connected RFID chip, EM4325, ensuring optimal performance. The simulation shows that the antenna input impedance is $Z_{\text{RFIDant}} = 7.8 + j113\,\Omega$ at

a frequency of 915 MHz. It matches the complex conjugate of the designed antenna to maximize the antenna efficiency.

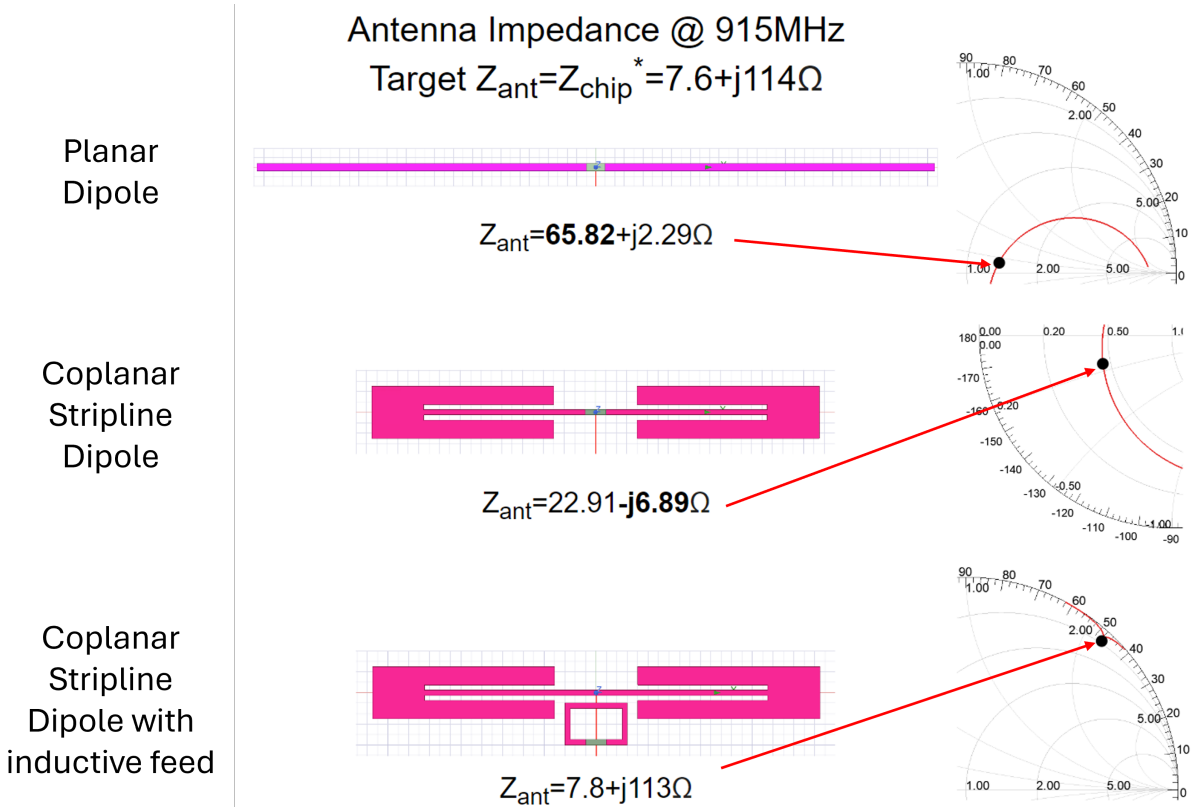

Fig. 3.4: Antenna matching design workflow for the RFID tag antenna of the UHF RFID sensing system presented in this thesis.

Once the antenna shown in Fig. 3.5 was designed and fabricated, its actual input impedance was measured to assess its performance in comparison to simulation. During the manufacturing process, several factors such as material imperfections, fabrication tolerances, or variations in the assembly can introduce errors that may affect the final characteristics of the antenna. As a result, the observed input impedance may deviate from the simulated results. Therefore, it is crucial to measure the antenna's actual input impedance and compare it with the simulation results to ensure it meets the design requirements.

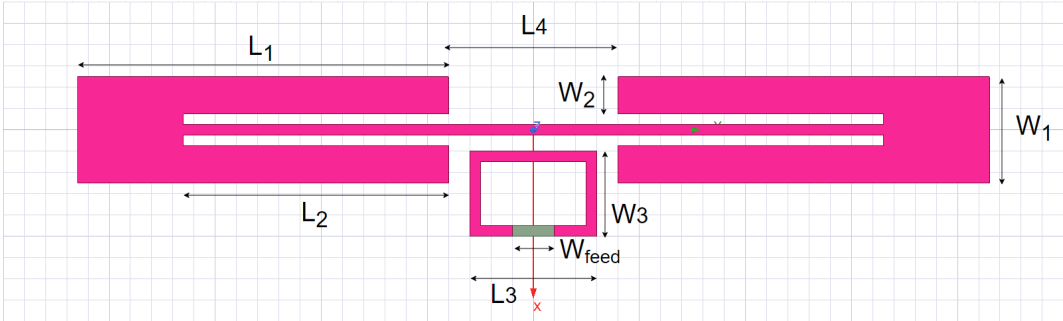

Fig. 3.5: Dimensions of the CPS Antenna (L_1=35 mm, L_2=25 mm, L_3=12 mm, L_4=16 mm, W_1=10 mm, W_2=3 mm, W_3=8 mm, W_{feed}=4 mm).

3.2.1 Impedance Measurement of The Designed RFID Antenna

There are different ways of measuring the impedance of the antenna. One method introduced in [56] involves using a 180° hybrid coupler. The two differential output ports that have a 180° phase difference on the 180° hybrid coupler are used to feed the antenna through two coaxial cables. The outer conductor of the two feeding cables are soldered together to create a common ground. The sum port of the coupler will match 50 Ω and the difference port will be directly connected to a vector network analyzer (VNA). The measured S_{11} parameter directly reflects the antenna impedance. This method offers a simple and straight-forward impedance measurement of a balanced antenna. However, the antenna for RFID tags are usually small and measurements are challenging due to the proximity effects introduced by any cable connection to the antenna, as this will affect the electric field distribution around the antenna. As a result, this method might introduce some inaccuracy in the measured antenna impedance.

To overcome the potential inaccuracy using the hybrid coupler and get more accurate impedance measurements for the designed CPS antenna, a half antenna test is used. The half-antenna test is a good approach to achieve accurate measurements. A half-antenna test

involves placing half of a balanced antenna over a finite ground that is theoretically infinite in size [57, 58]. This setup utilizes image theory and allows the ground plane to act as a mirror. The antenna will behave like a full antenna, but the measured antenna impedance will be half of that of the full antenna. Using a finite ground plane minimizes ground effects and approximates ideal reflection conditions, providing accurate measurements of parameters like impedance and radiation pattern. This method is applied in this research to measure the impedance of the antenna. Figure 3.6 shows the setup of this method, where a half antenna is positioned above a ground plane that is much larger compared to the antenna's size. The feeding port of the half-antenna is soldered to an SMA connector and connected to a vector network analyzer for measurements. The measured real and imaginary parts over the frequency range of 700 MHz to 1.1 GHz are shown in Fig. 3.7. The impedance displayed in this graph corresponds to the half-antenna, which is half of the full antenna's impedance. At the operating frequency of 915 MHz, the measured antenna input impedance is $Z_{\text{IDant,measured}} = 10.8 + j110\,\Omega$.

3.3 Power Harvester Antenna Design

In the power harvester section of the sensor tag, a meandered dipole antenna, as illustrated in Fig. 3.8, is utilized to capture ambient RF energy radiated by the reader. There are a few specifications for designing the power harvesting antenna. The power harvesting antenna requires specific design considerations to optimize its performance. The gain needs to be high to increase the efficiency of the overall RF power harvesting section. Similar to the RFID antenna design, this antenna design begins with a half-wavelength dipole structure. Since both the RFID antenna and the power harvester antenna are linearly polarized and

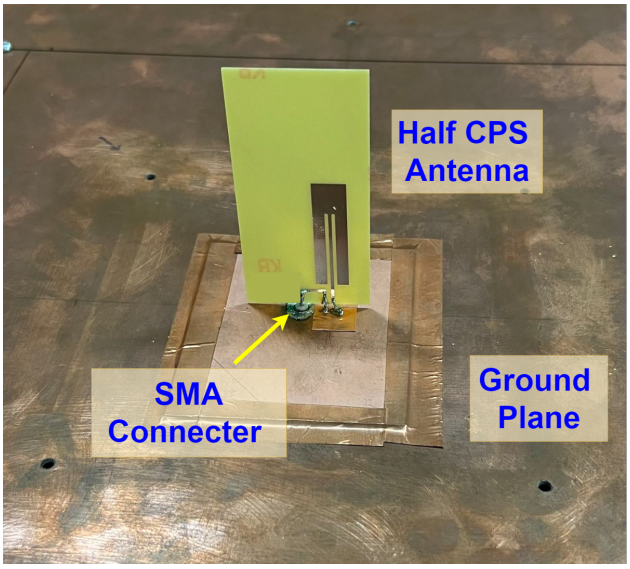

Fig. 3.6: Half CPS antenna setup for impedance measurement.

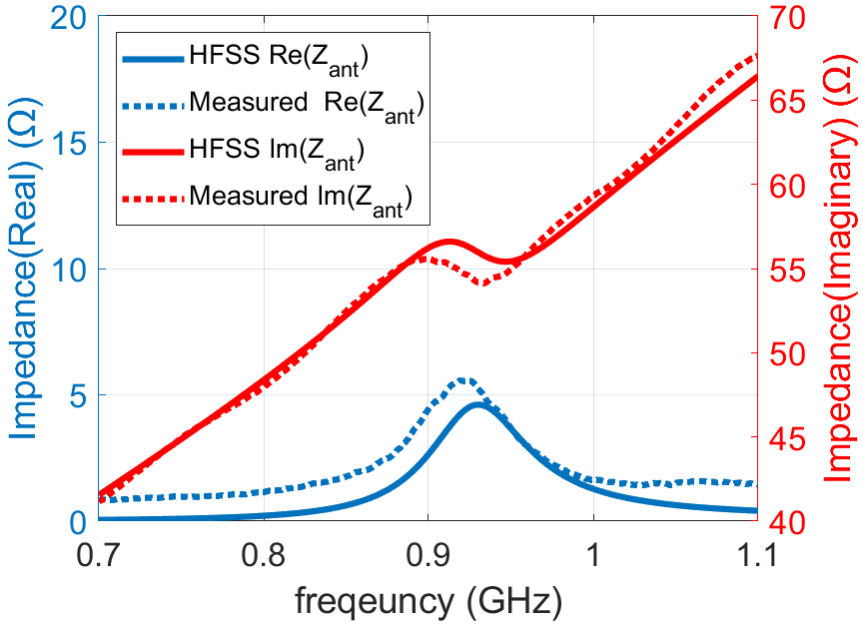

Fig. 3.7: Measured antenna impedance of CPS antenna design for RFID tag. The measured input impedance of the half antenna was multiplied by a factor of 2 to determine the input impedance of the CPS antenna shown in this figure.

both of them are an important part in the sensor tag, to prevent interference with the RFID antenna, they are oriented orthogonally, ensuring that the operation of the power harvester antenna does not compromise the RFID tag's functionality.

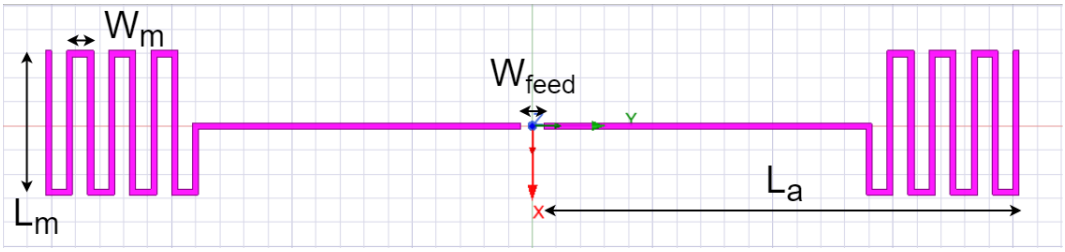

Fig. 3.8: Dimensions of meandered dipole antenna desing for RF power harvesting (L_a=39.5 mm, L_m=12 mm, W_m=2.25 mm, W_{feed}=2 mm)

To reduce the size of the overall antenna and minimize the loss of antenna gain, a meandered section is added to the end of each side of the half wavelength dipole antenna. The power harvester circuit P2110B has an input impedance that matches to 50Ω. This characteristic provides flexibility for designing the antenna. The antenna is designed to have a minimal imaginary part (close to zero). Subsequently, a quarter wavelength transmission line method is employed to match the real part of the designed antenna to 50Ω.

3.3.1 Impedance Measurement of The Desiged Power Harvester Antenna

The RF power harvester antenna is fabricated on an FR4 substrate with a thickness of 0.6 mm and relative permittivity of 4.4. Half-antenna test is used to measure the actual antenna impedance of the RF power harvester antenna. The harvester antenna is simulated using Ansys HFSS and the simulated input impedance is $Z_{\text{EHant}} = 34.9 + j0.1\,\Omega$ at a frequency of 915 MHz. The measured real and imaginary parts over the frequency range of 850 MHz

to 950 MHz are shown in Fig. 3.9. The impedance displayed in this graph corresponds to the half-antenna, which is half of the full antenna's impedance. At the operating frequency of 915 MHz, the measured antenna input impedance is $Z_{\mathrm{EHant}} = 26.7 + j7.04\,\Omega$ shown in Fig. 3.10. The measured antenna impedance is close to simulated one. Differences in the actual material properties (like dielectric constant and loss tangent of substrates) versus those assumed in simulations can cause discrepancies in impedance. To match the input impedance of the harvester antenna to the RF power harvester, a one to one balun is used to convert the unbalance input to balanced input. The balun used in this thesis has a insertion loss of 2 dBi, a 1:1 impedance ratio and $4.5 - 3000$ MHz bandwidth. To match the antenna to the power harvester a quarter wavelength stripline matching technique is applied in this thesis, the length is designed to be quarter wavelength. The characteristic impedance of the stripline can be calculate by using

$$Z_{line} = \sqrt{Z_{ant} Z_0} = \sqrt{35 \times 50} = 41.8\Omega \tag{3.2}$$

where Z_{ant} is the input impedance of the meandered dipole and Z_0 is the input impedance of the RF power harvester. The final fabricated antenna incorporated with the balun and the matching stripline is shown in Fig. 3.11.

One of the most important parameter for the power harvester antenna is the antenna gain. For a meandered dipole antenna, its small size makes it suitable for designing a more compact sensor tag. However, the gain will be lower than a half wavelength dipole antenna. To determine the gain of the antenna, a relative antenna gain measurement was done in the RF Lab at the University of Manitoba. A relative antenna gain measurement is helpful when we know the gain of the reference antenna. The detailed setup is shown in Fig. 3.12,

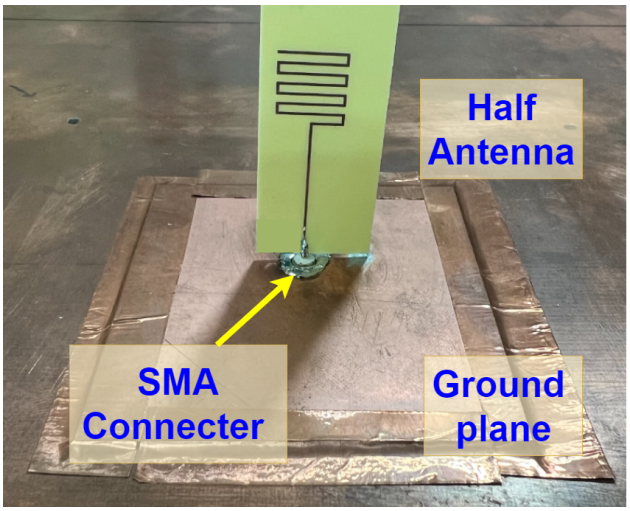

Fig. 3.9: Half meandered dipole antenna setup for impedance measurement.

that consists of a 2.5 dB Yagi antenna used as the transmitter, a commercial monopole antenna with an average antenna gain around 0.5 dBi, and the designed meandered dipole antenna. A VNA is used to measure the S_{21} of the experimental setup. The Yagi antenna is connected to port 1 of the VNA. Port 2 of the VNA is connected to a commercial monopole antenna with a known gain. The power received at port 2 will be saved and compare with the result obtained by connecting a meandered antenna to port 2. The S_{21} measurement for both antenna are shown in Fig. 3.13 The S_{21} measurement result for the known monopole is around -23.15 dB at 915 MHz. The S_{21} measured for the designed meander line is around -22.52 dB at 915 MHz. Based on the measurement, it shows the designed antenna has a gain of around 1 dBi.

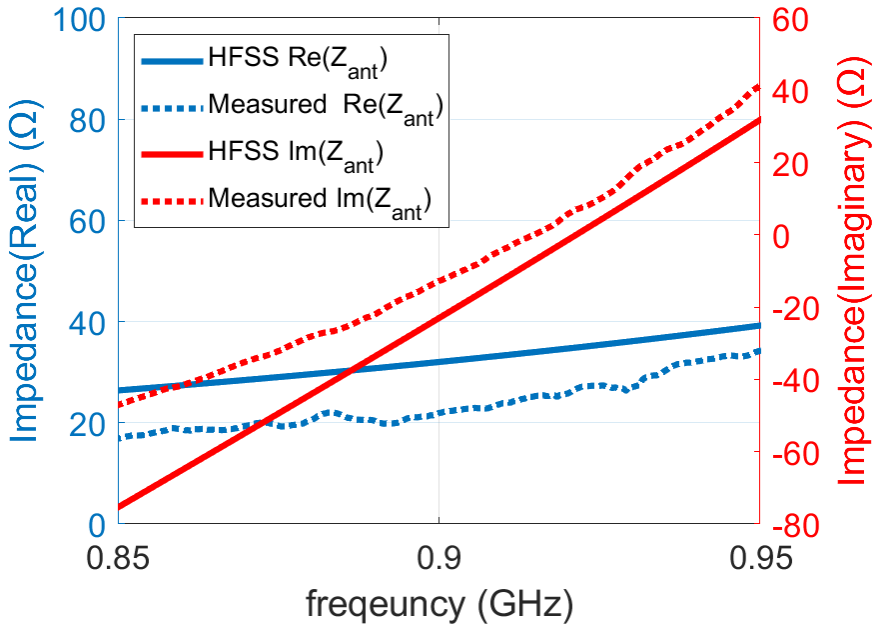

Fig. 3.10: Measured input impedance of the meandered dipole antenna designed for the power harvester. The measured input impedance of the half antenna was multiplied by a factor of 2 to determine the input impedance of the dipole antenna shown in this figure.

3.4 Summary

In this chapter, both the RFID antenna and RF power harvester antenna design was presented. The design approach and the procedure were explained in details. The dimensions of both antennas were presented. Both antennas were fabricated on an FR4 substrate with a thickness of 0.6 mm and relative permittivity of 4.4. Both antennas were tested using half antenna testing method to find out the actual antenna's input impedance. The antenna gain of the power harvester antenna is measured using a relative antenna gain method. The gain measured is around 1 dBi. The next chapter covers the selection of magnetic field sensor and the detailed testing method to evaluate the performance of different magnetic field sensors.

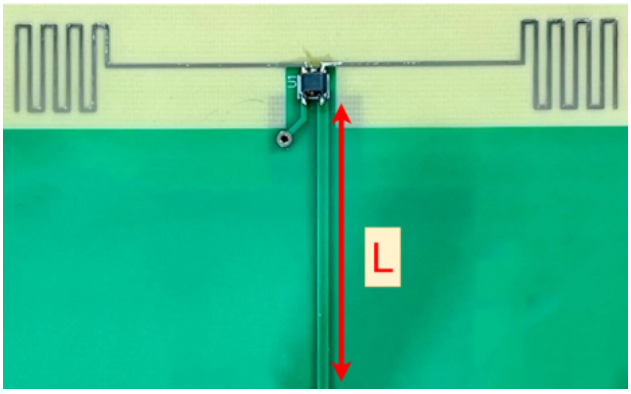

Fig. 3.11: Fabricated meander-line dipole antenna incorporating a 1:1 balun and a quarter wavelength microstrip line for matching the power harvester antenna to the RF power harvester.

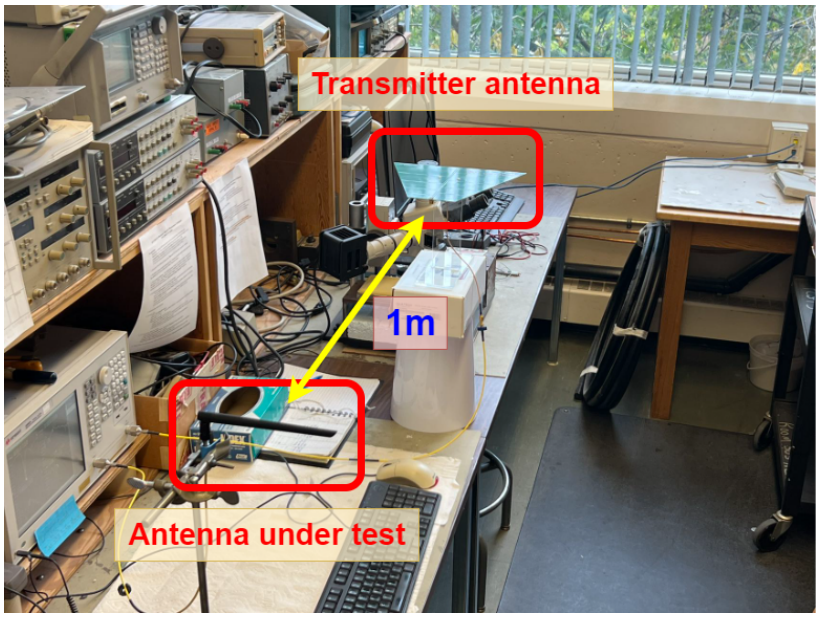

Fig. 3.12: Experiment setup for antenna gain measurement.

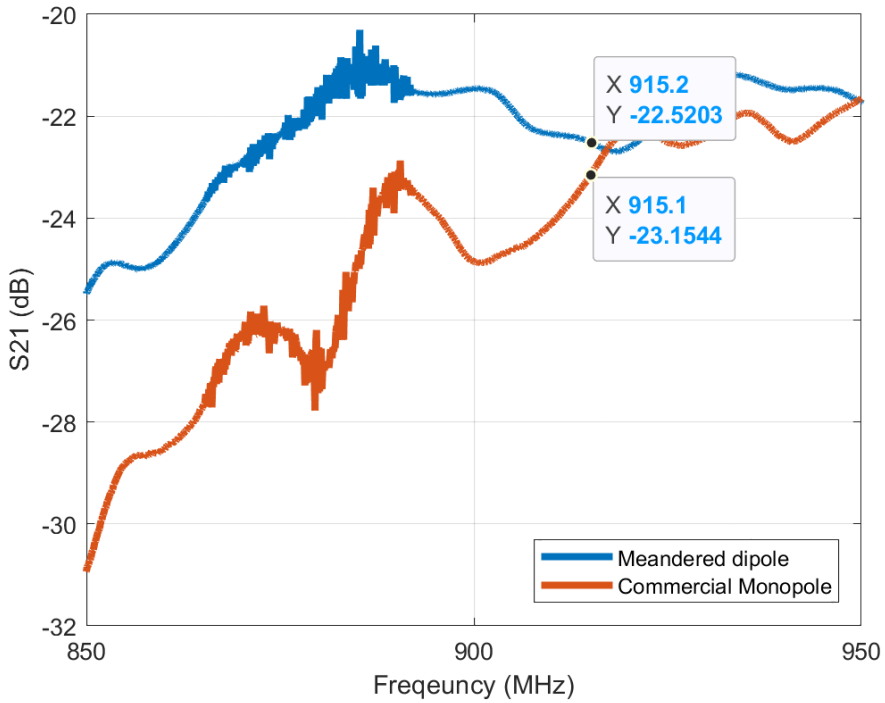

Fig. 3.13: Measured S21 parameter for commercial monopole antenna and the fabricated meandered dipole antenna. The difference at $915.2\,\text{MHz}$ indicates the gain difference.

Chapter 4

Experimental Evaluation of Magnetic Field Sensors

Achieving accurate magnetic field measurements on an overhead HVdc transmission line requires selecting the appropriate magnetic field sensor is essential. The sensor must have high sensitivity and a wide linear range. Additionally, it needs to operate reliably in harsh environments, including fluctuating weather conditions, temperature variations, and electromagnetic interference from nearby power equipment. Low power consumption is also important, as the power transmitted from the RFID reader is limited by the standards of the RFID system. Finally, compatibility with data acquisition systems and signal processing equipment is crucial for precise monitoring and analysis of the magnetic field behavior around the HVdc line. In this thesis, two different types of magnetic field sensors are evaluated to determine the most suitable option for integration with the RFID tag.

A solenoid is used to generate a known magnetic field to test the two different magnetic field sensors. The solenoid has 3400 turns and a dc resistance of 66.5Ω. The solenoid is

powered by a 30 V/6 A power source. At maximum voltage of 30 V, the current of the solenoid is 0.45 A, generating a maximum magnetic field of 14 mT. The measured data is recorded in voltage, and a MATLAB program is used to calculate the actual magnetic field. The calculated field from the sensor measurements will be compared with results from an electromagnetic simulation. The simulation is done using the magnetostatic module of a commercial simulation software COMSOL multiphysics. The specification of the solenoid listed in Table 4.1 is used to build the solenoid in COMSOL multiphysics (See Fig. 4.1).

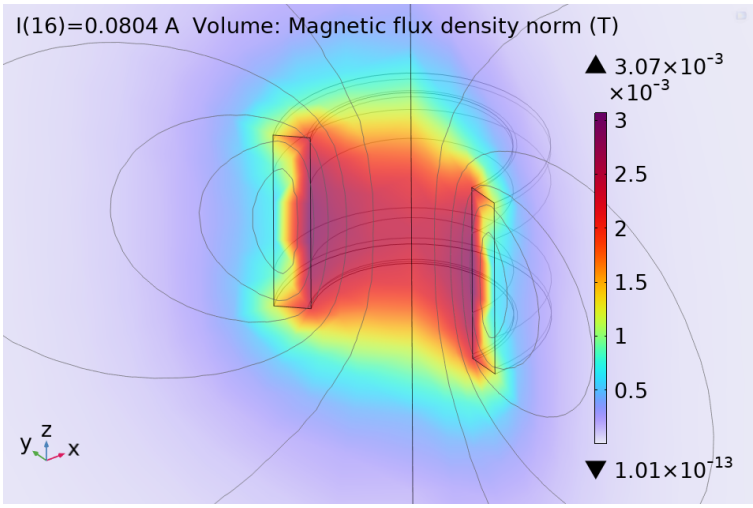

Fig. 4.1: Solenoid simulation with varying current using COMSOL Multiphysics.

Table 4.1: Technical parameter of the solenoid used in this thesis for testing magnetic field sensors.

Length	9 cm
Inner diameter	9.2 cm
Outer diameter	12.6 cm
Wire gauge number	AWG22
Number of turns	3400 turns
DC resistance	66.5Ω

4.1 Ratiometric Linear Hall Effect Sensor

The primary choice for magnetic field sensing in this thesis is a Hall-effect sensor. The basic output of a typical Hall sensor is a potential difference generated across the sensor surface by the external magnetic field. For this thesis, the DRV5055 Hall effect sensor is used. DRV5055 A1 has a full-scale range of ±21 mT, which is much larger than the field generated by an overhead HVdc transmission line and the sensing bandwidth of DRV 5055 is 20 kHz [59]. The output noise is 12 mV, which corresponds to a magnetic flux density measurement resolution of 0.12 mT. To test a Hall effect sensor with a solenoid, no additional amplification is required since the field is relatively strong. The maximum magnetic field from an HVdc line is around 4 mT. The Hall effect sensor is tested using the setup shown in Fig. 4.2.

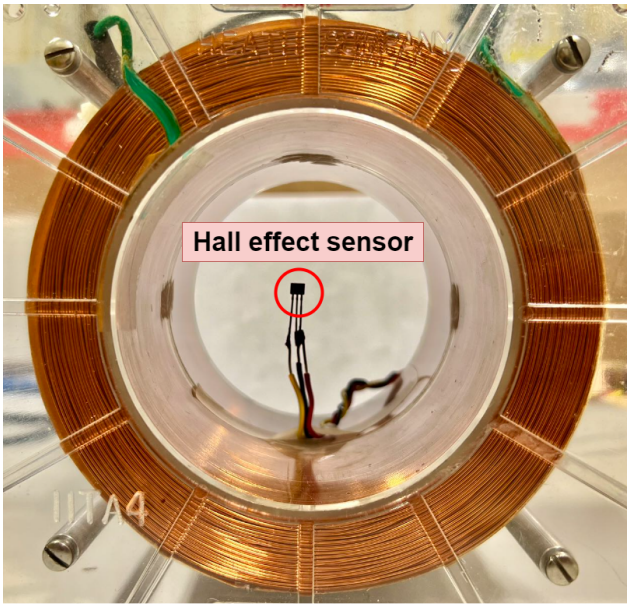

Fig. 4.2: Experimental setup for Hall effect sensor which consists of a solenoid and a Hall effect sensor.

Table 4.2: Hall effect sensor output and the equilvalent magnetic flux density with varying current intensity.

Current	Average Vout	Average Magnetic field (mT)	Simulation
0 A	2.48 V	0 mT	0 mT
0.1 A	2.79 V	3.1 mT	2.982 mT
0.2 A	3.08 V	6.0 mT	5.9645 mT
0.3 A	3.39 V	9.1 mT	8.9481 mT
0.4 A	3.67 V	11.9 mT	11.931 mT
0.47 A	3.88 V	13.9 mT	14.019 mT

The sensor's calibration factor is 99.62 mV/mT, which is very close to the 100 mV/mT specified in the datasheet. The standard deviation is minimal, as there are no additional components in this test setup. The only possible sources of noise are the sensor itself and the multimeter. Because the magnetic field is static, it remains constant during measurement at a given current. According to the datasheet, the typical noise level is approximately 6 mV, corresponding to 0.06 mT. Finally, Fig. 4.3 shows the linearity and the dynamic range of the Hall effect sensor.

4.2 Magnetoresistive Magnetic Field Sensor

The second choice for magnetic field measurement is a magnetoresistance sensor, which consists of four magnetic field-dependent resistors in a bridge circuit configuration. The output of this bridge circuit represents the magnetic field across the sensor. The full-scale range for magnetic field measurement is ±0.6 mT, which is smaller compared to the Hall effect sensor. With an input voltage of 5 V, the sensor has a sensitivity of 50 mV/mT, an instrumentation amplifier with a gain of 42 is used to amplify the signal for measurement [21]. An instrumentation amplifier is chosen for its low common-mode rejection ratio, which helps

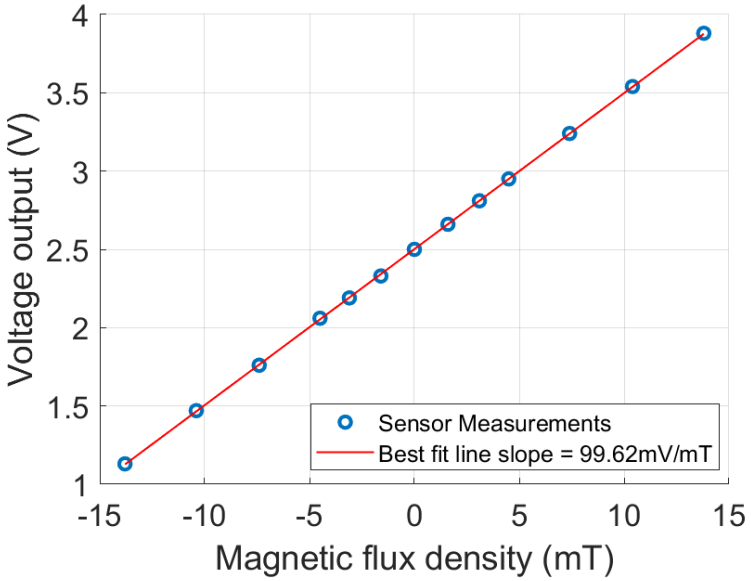

Fig. 4.3: Magnetic response of DRV 5055 Hall effect sensor.

minimize interference. A critical aspect of using a magnetoresistance sensor is the set/reset pulse circuit, as the sensor requires a set/reset pulse to produce an output. According to the datasheet, the set/reset pulse should have a 0.5 A amplitude, 0.1% duty cycle, and a 1.5 μs pulse. To generate this pulse, a series RC circuit and a power MOSFET are used to drive the pulse to the sensor's set/reset pin. The MOSFET gate is controlled by a signal generator to achieve the desired 0.1 % duty cycle. The RC values are set to 200 Ω and 0.22 μF, with the capacitor charged to 5 V. Although the measured resistance of the positive and negative reset / reset pins is 7 Ω, resulting in a current of 0.71 A which does not match the typical values, but these values still fall within the acceptable current range specified in the sensor datasheet.

Figure 4.4 shows the circuit to drive the magneto-resistance sensor, where the acutual circuit was built on a breadboard. The same solenoid used for testing the Hall effect sensor is

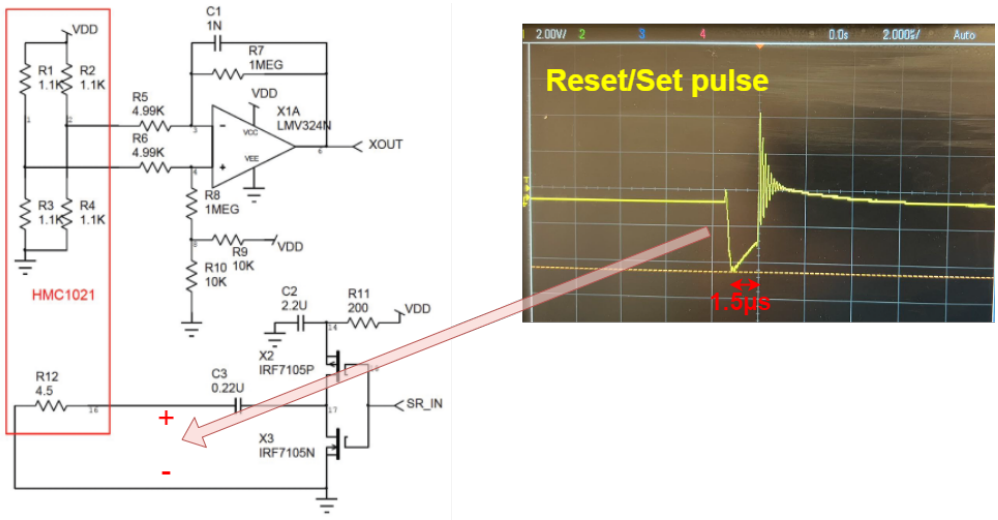

Fig. 4.4: Circuit diagram to operate a magnetoresistve sensor and the Set/Reset pulse needed for each magnetic field measurements.

used to test the magneto-resistance sensor. The magnetoresistance sensor does not have the standard 2.54 mm pin-to-pin distance, so it is soldered onto an adapter to enable connection to a breadboard. Since the full scale of the the magneto-resistance sensor is much lower than the Hall effect sensor, the current of the power supply was limited to ensure the magnetic field will not go above 0.6 mT. The magnetoresistance sensor was tested, using both a DC power source and a 0.5 Hz ramp wave from a signal generator. The RC circuit provides a 4.89 V set pulse and a -3.89 V reset pulse, each with a duration of around 1.5 μs.

Table 4.3: Magnetoresistive sensor output and the equilvalent magnetic flux density with varying current intensity

Current	Average Vout (V)	Average Magnetic field (mT)	Simulation
0 A	0 V	0 mT	0 mT
0.01 A	0.85 V	0.37 mT	0.29827 mT
0.02 A	1.31 V	0.58 mT	0.59645 mT
0.03 A	1.64 V	0.729 mT	0.89481 mT

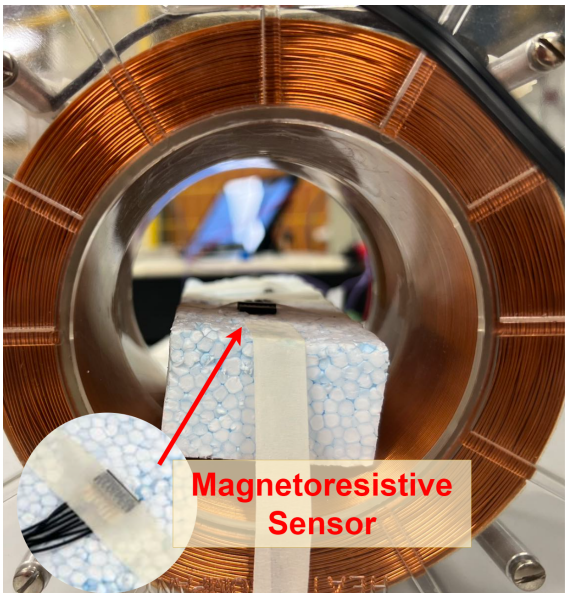

Fig. 4.5: Experimental setup for magnetoresistive sensor which consists of a solenoid and a magnetoresistive sensor soldered on an connector.

The measured data shown in Table 4.3 from the magnetoresistance sensor is not as accurate as that from the Hall effect sensor. While the measured field is close to the simulation, it is not as precise as the Hall effect measurements. Surprisingly, the measured data has a very stable output, with a standard deviation almost zero. One of the main problems with the magnetoresistance sensor is the hysteresis error. The hysteresis is evaluated using a 0.5 Hz ramp wave. At the end of each cycle, the output does not return to the 0 V point. This behavior is consistent with the hysteresis error specified in the datasheet, which is around 0.24 V. This is typical behavior when the sensor crosses a 0.3 mT field.

Finally, the measured voltage of the output of the bridge circuit versus the magnetic field is converted to a graph, shown in Fig.4.6. The graph matches the behavior listed in the datasheet for the HMC 1021Z. The linear range of this sensor is around 0.6 mT (6 Gauss or

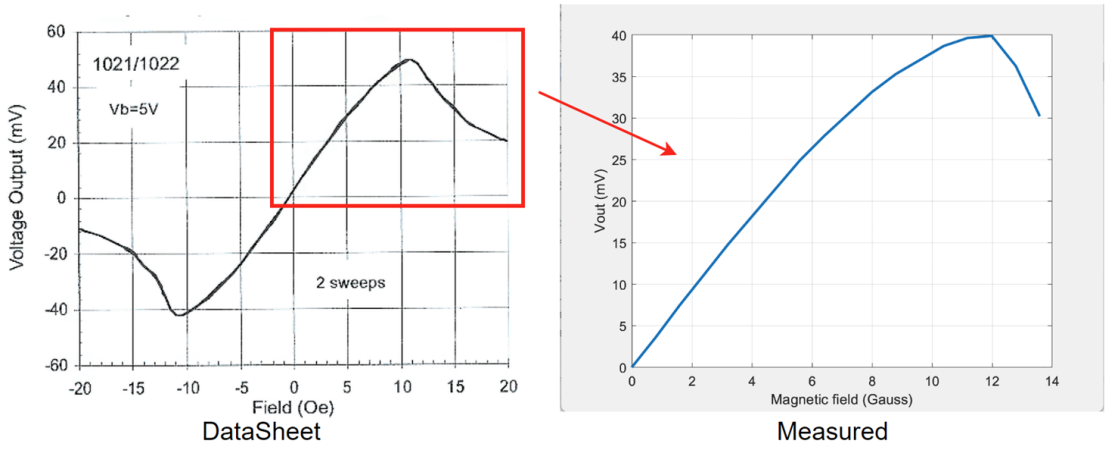

Fig. 4.6: Magnetic response of HMC 1021Z-RC magnetoresistance sensor.

6 Oersted), and after about 1 mT, the sensor begins to exhibit nonlinear behavior, as shown in Fig. 4.6.

4.3 Summary

In this chapter, two different types of commercial magnetic field sensors are tested using a solenoid to generate a wide range of magnetic field intensities. The Hall effect sensor demonstrates high accuracy and a wide linear range for measuring magnetic fields. It is capable of measuring fields up to 14 mT with a sensitivity of 100 mV/mT. The magnetoresistive sensor, while highly sensitive, has a linear range of only up to 0.6 mT, which is much lower than the magnetic field levels around HVdc lines. Furthermore, an extra power budget is required since the sensor needs to be driven by MOSFETs and operational amplifiers. The increase in power usage reduces the performance of reading ranging of the sensor significantly. After comparing the characteristics of the two sensor types, the Hall effect sensor is chosen for the implementation of the RFID-based magnetic field sensor.

Chapter 5

Energy Transfer and Harvesting System

The core of energy management in wireless RFID sensor systems consists of two parts, the power transmitter, which is a UHF RFID reader in this thesis, a power harvester with an integrated power management circuit. The UHF RFID reader is responsible for generating and transmitting RF energy to create a stable energy source for the RFID based magnetic field sensor. In parallel, the power harvester is used to capture this radiated RF energy and converting it into DC power through high-efficiency RF-to-DC conversion techniques. The power management component controls the distribution of harvested energy, ensuring voltage stability and managing energy storage. This approach offers intermittent measurement, which is acceptable for measuring a dc magnetic field. This approach eliminates the need for traditional power sources such as a battery.

5.1 Power Transmitter-UHF RFID Reader

An RFID reader is a device that is used to communicate with RFID tags in order to read or write data stored on them. It works by emitting RF waves that power up passive RFID tags and receive the backscattered modulated wave from the RFID tags. The reader decodes the unique identification code of the tag or other stored data, and it can also be used to write new information to tags that has a writable memory. RFID readers operate in various frequency ranges, such as low-frequency (LF), high-frequency (HF), and ultra-high-frequency (UHF).

An RFID reader typically consists of three main components: an antenna, a transmitter module, and receiving demodulation module as shown in Fig. 5.1. The antenna is responsible for emitting radio signals and receiving the backscattered signals from RFID tags. The transmitter is an RF source that generates a signal within the selected frequency band. The receiver includes a signal amplifier, a mixer, a filter, and a demodulator. The received signal is amplified and down-converted before being demodulated.

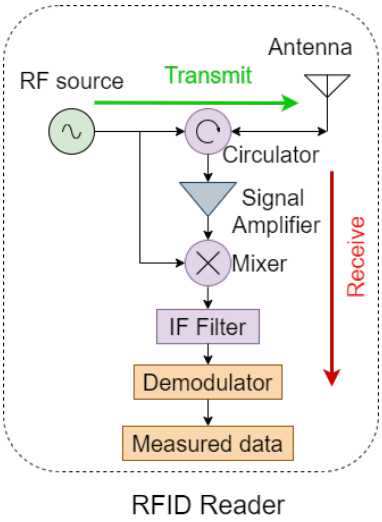

Fig. 5.1: Block diagram of an typical RFID reader include the signal path for transmitting (Green) and receiving (Red).

The RFID reader used in this thesis is called the USB-Plus-Nano, featuring the ThingMagic Nano module. This RF module is recognized as one of the most accurate and consistent options available commercially, making it an excellent choice for precise RFID applications. The specifications for the USB-Plus-Nano RFID reader and the ThingMagic Nano module are outlined in Table 5.1. These specifications include key parameters such as power consumption, operating frequency, interface protocol, and the working frequency design for use in North America. Together, these features contribute to the performance and reliability of the RFID system, ensuring effective data acquisition and processing in various applications.

Table 5.1: Technical specifications of the commerical RFID Reader USB-Plus-Nano.

Technical Specifications	
Operating Voltage	5.0 V
Operating Current	$< 700\,\text{mA}$ (reading) $< 5\,\text{mA}$ (sleep)
Air Interface Protocol	EPCglobal UHF Class 1 Gen 2 / ISO 18000-6C
Operating Frequency	902-928 MHz
Operating Area	FCC (NA, SA) $915 - 928$ MHz
Antenna Gain	2 dBi
Output Power	0-27 dBm
Output Accuracy	+/-1 dbm

5.1.1 Transmitted Power Test Procedure and Results

The RFID reader is tested in the RF laboratory of the University of Manitoba. The test setup includes a wide-band Yagi antenna, an RFID reader, and a spectrum analyzer. The Yagi antenna is a wideband antenna with a gain of 2.5 dBi that operates in the range of 300 MHz to 1.1 GHz. The antenna is used as a receiving antenna connected to the spectrum analyzer to receive the RF wave emitted by the RFID reader. The test setup is shown in

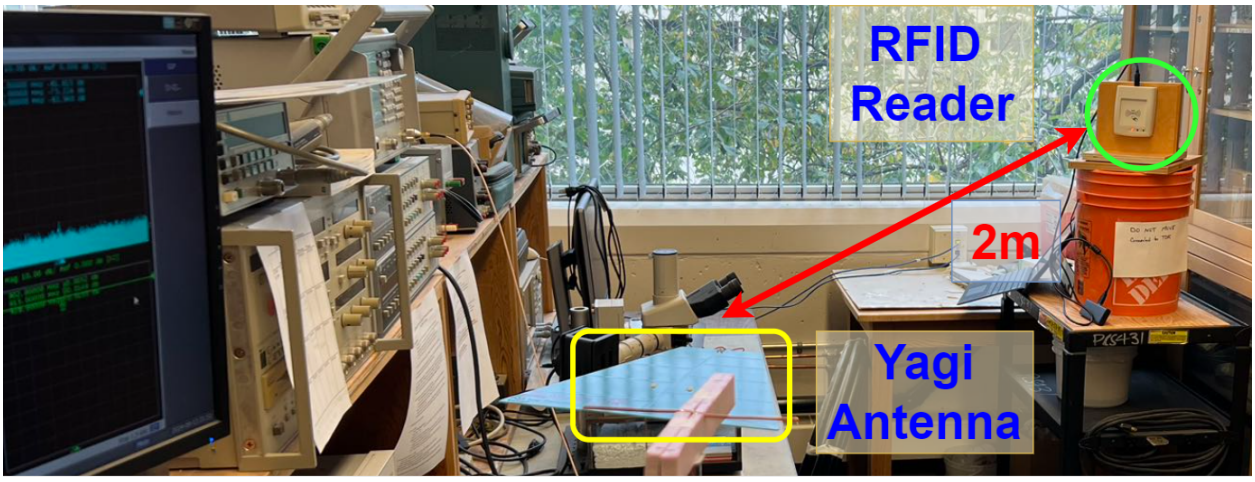

Fig. 5.2: Experiment setup for measuring the RF output of a RFID reader.

Fig. 5.2. The RFID reader is placed 2 m from the Yagi antenna at the same height. The RFID reader is configured to operate within the frequency range used in North America ($915 - 928$ MHz) [32]. The power level of the reader is set to 0 dBm. The power received by the Yagi antenna is shown in Fig. 5.3, the signal is between $916 - 928$ MHz which matches the datasheet. The expected received power level can be calculated using [54]

$$P_r^T = \text{EIRP}\left(pzG^T\right)\left(\frac{\lambda}{4\pi d}\right)^2 = -25.4\,\text{dBm} \tag{5.1}$$

where EIRP is the equivalent isotropic radiated power, p is the polarization efficiency, z matching coefficient, G^T is the gain of the RFID tag antenna, λ is the wavelength in free space, and d is the distance between the RFID reader. The received power level is -25.18 dBm. The measured power spectrum shows that the RFID reader matches the specifications listed in its datasheet. Because the Yagi antenna is a wideband antenna, it is affected by interference from other wireless devices like WiFi and Bluetooth in the environment, as well as by multipath signals, which can cause minor mismatches.

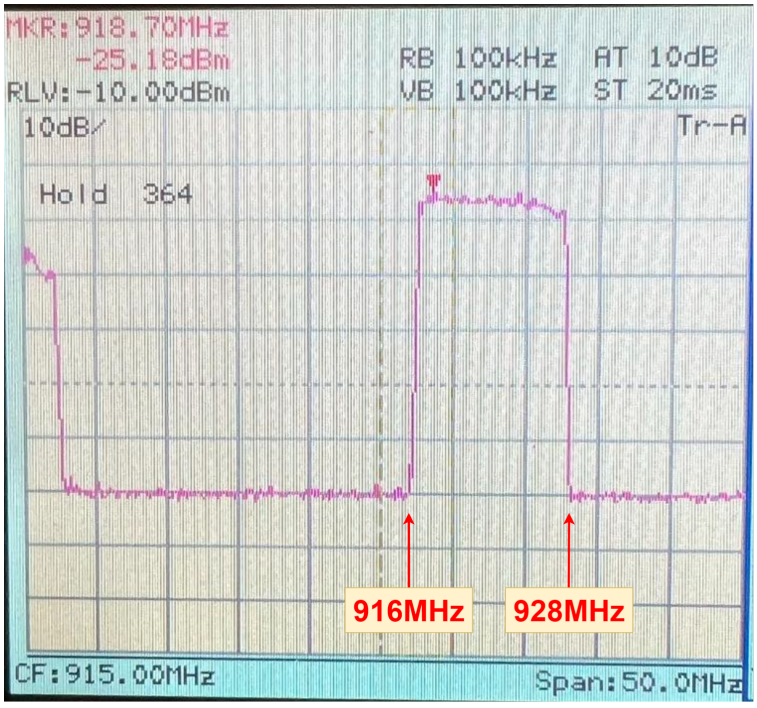

Fig. 5.3: Measured power spectrum from the RFID reader.

5.1.2 Reading Range and Received Signal Strength

In Section 5.1.1, the transmit power is measured and compared with a theoretical value. To obtain information from the RFID-based sensor, the signal power level received by the RFID reader is also important. The received signal strength (RSS) determines the effective communication distance and quality between the RFID reader and the sensor tag. The RSS is determined by the several parameters of the RFID communication system including reader and tag antenna, path loss, modulation index of the RFID chip, polarization of the antenna, and the effective power of the transmitter. There are also effects from environmental interferences. A minimum RSS threshold is normally called minimum detectable signal (MDS). The RSS must be higher than MDS in order to be detected by the RFID reader. The MDS is usually the limiting factor of the maximum reading range. Path loss is the most significant factor that influences RSS and reading range. In free space, the received power at a distance d from the transmitter can be approximated using [54]

$$\mathrm{RSS} = G_r^R G_t^R \left(pzG^T\right)^2 \left(\frac{\lambda}{4\pi d}\right)^4 |e|^2 P_t \tag{5.2}$$

where G_r^R and G_t^R are the gains of the RFID reader's transmitter and receiver antenna, respectively, p is the polarization efficiency, z is the matching coefficient, G^T is the gain of the RFID tag antenna, λ is the wavelength in free space, d is the distance between the RFID reader and tag, e is the modulation index, P_t is the transmitter power. To verify the actual RSS and the reading range of the RFID reader, an experiment was conducted at the antenna lab using the setup shown in Fig. 5.4.

The RFID reader is the same as introduced in Section 5.1.1. The RFID tag used is a commerical UHF RFID tag with a impinj Monza 5 RFIC. The distance is varied from 0.7 m

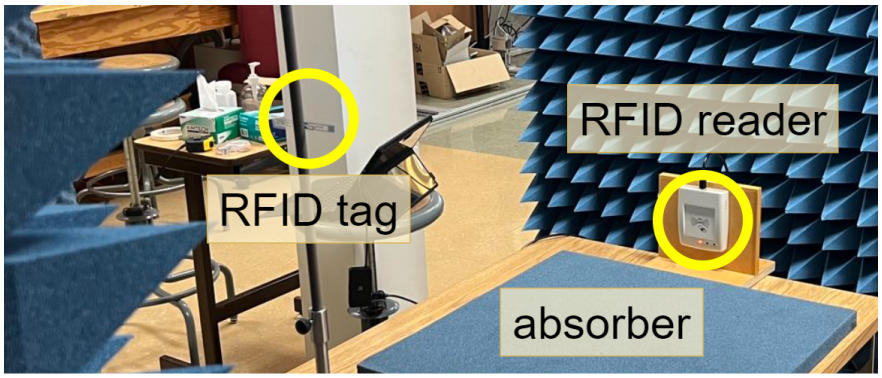

Fig. 5.4: Experiment setup for measuring the reading distance and RSS.

to 1.3 m. Figure 5.5 shows the measured RSS at distances ranging from 0.7 m to 1.3 m. The measurment is then compared with the result computed using equation 5.2. As the distance increases, the two curve start to converge. The reason might be that, at shorter distances, the two antennas are in their near field region, whereas (5.2) assumes operation in the far-field region. As the distance increases, the RFID tag enters the far-field region, where the measurement and theoretical values become closer to each other.

5.2 RF Power Harvesting Integrated Circuit

In the power management design part, some characteristics of P2110B are extensively used in the sensor tag design. The most important feature of the P2110B is its ability to harvest ambient RF energy with a harvesting antenna and converting it into dc power with high efficiency, typically over 80% [60]. The detailed specification of P2110B is presented in Appendix B. The harvested dc power is stored in an external supercapacitor, which is selected to be 10 mF to ensure a stable power supply. This supercapacitor provides a reliable energy reservoir, allowing the sensor tag to maintain consistent operation with the help of a power

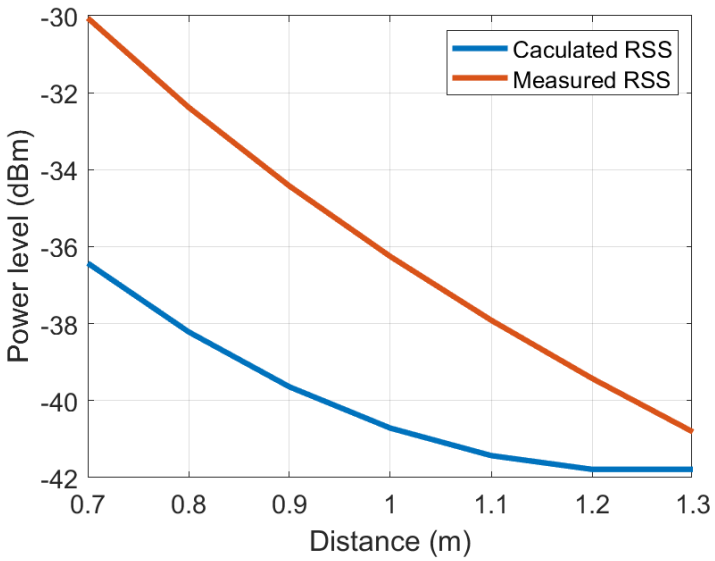

Fig. 5.5: Received signal strength for different distances.

regulator. Another important aspect of the P2110B is its built-in power management system, which includes a low-dropout (LDO) voltage regulator. This regulator controls the power output by holding it off until the supercapacitor's voltage reaches a threshold of 1.25 V, as illustrated in Fig. 5.6. Once the capacitor reaches this charge level, the power supply starts, enabling the tag's components to operate. However, if the capacitor's voltage falls below 1 V, the P2110B will cut off power to the components. This regulated switching ensures that the sensor tag's circuit remains powered only when sufficient energy is available. The total energy accumulated in the capacitor during charging is critical to sustaining operations during periods without RF energy. The available energy E_T can be calculated by using

$$E_{\mathrm{T}} = \frac{1}{2} C_{\mathrm{ext}} (V_{cap,max}^2 - V_{cap,min}^2) = 2.8125\ mJ \tag{5.3}$$

where C_{ext} is the supercapacitance (10 mF), and $V_{\text{cap,max}}$ and $V_{\text{cap,min}}$ are the maximum voltage to start sensor operation and the threshold voltage respectively. This is the maximum energy that can be consumed during the magnetic field measurement process. This energy calculation informs how long the sensor tag can operate autonomously, which is especially useful for applications with intermittent RF power sources. The operation time is given by [60]

$$t_{ON} = \frac{C_{ext}}{15 V_{out} I_{out}} \approx 60ms \tag{5.4}$$

During the operation time, the operation done is shown is Fig. 5.7. After the 24.5 s initial charge time, the power supply will start. The program will keep measuring the magnetic field for 10 ms, and then the writing will start. The program begins by converting the analog voltage from the sensor into a digital value. Once the digital measurement is obtained, the program enables the write function to initiate communication with the RFIC. It specifies the target address within the RFIC memory and writes the digital measurement data to this address. After completing the data transfer, the program disables the write function to prevent further unintended modifications and ensure proper operation. The entire process takes about 5 ms and will be repeated 8 times. The power will be turned off once the capacitor value drops below 1 V. After a 5 s recharge time, the cycle will start over again.

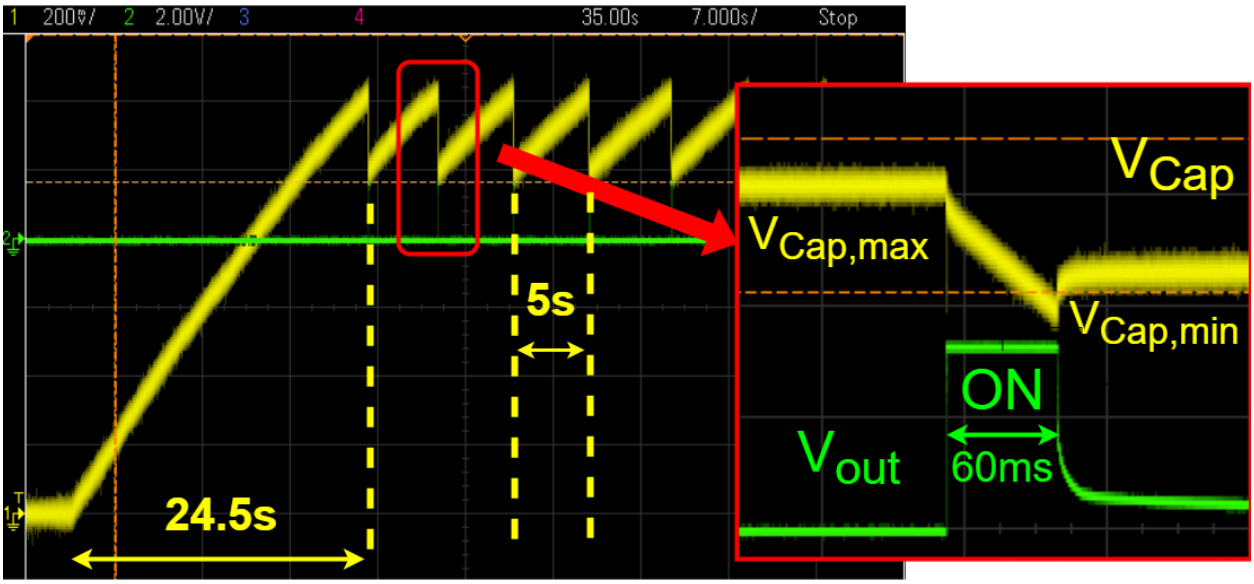

Fig. 5.6: Scope measurement of the operation of the UHF RFID based magnetic field sensor.

5.3 Summary

In this chapter, the power transmitter (RFID reader) used in this thesis is tested. A commercial UHF RFID tag is used to evaluate the reading range and received signal strength of the RFID reader. A wideband antenna measures the power level and frequency band of the transmitted wave. Details of the RF power harvester P2110B used in this thesis are provided, and its output waveform is measured using an oscilloscope. A cold-start charging time of 24.5 s and a recharging time of 5 s are achieved. The timeline of the measurement operation is shown. In the next chapter, the final fabricated UHF RFID system is shown. Experiments were done to validate the capability of the designed system.

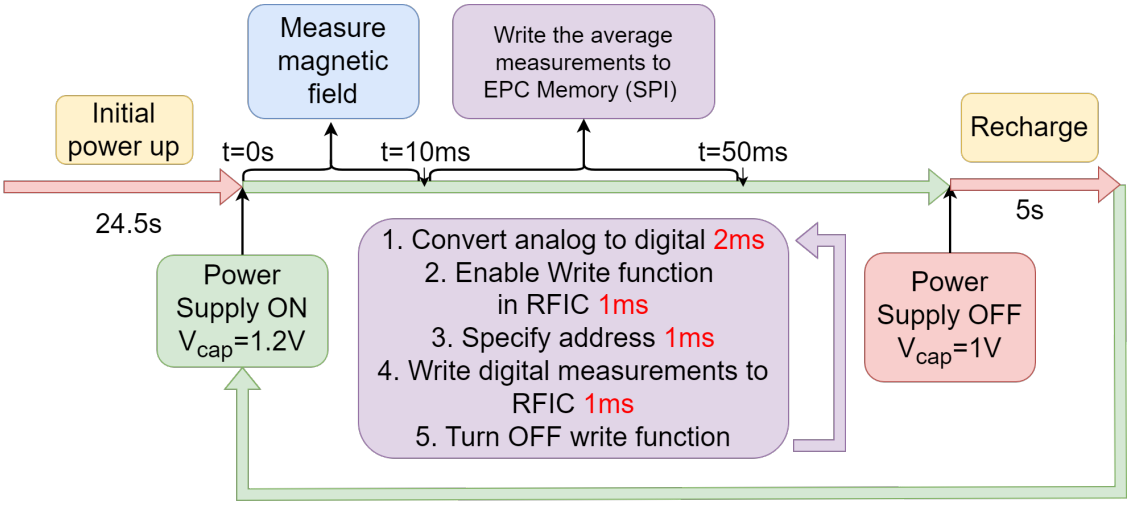

Fig. 5.7: Operation timeline after charging is complete. During the 60 ms window of the "ON" time, the microcontroller waits 10 ms for the output of the Hall effect sensor to stabilize. A time of 5 ms is needed to convert the analog voltage to digital and store the value. This is repeated 8 times and the average of the 8 readings are written to the RFIC. After completing the data transfer, the program disables the write function to prevent further unintended modifications and to ensure proper operation.

Chapter 6

Performance Characterization of the Fabricated Magnetic Field Sensor

6.1 Fabricated Sensor

Figure 6.1 shows the fabricated UHF RFID-based magnetic field sensor. it comprises two linear polarized antennas presented in Chapter 3, a microcontroller, the Hall effect magnetic field sensor, and the RF power harvester, P2110B. This integrated configuration enables efficient communication, data processing, and precise magnetic field sensing within a compact and streamlined design. The power harvester presented in Section 5.2 is used to capture energy from electromagnetic waves emitted by an RFID reader. This harvested energy is converted into stable dc output and stored in the 10 mF supercapacitor. The embedded power management circuit controls the flow of power to both the magnetic field sensor and the microcontroller. The Hall effect sensor captures magnetic field data and generates a voltage corresponding to the magnetic field. This voltage is then sent to the microcontroller's

analog-to-digital converter (ADC) for processing. The microcontroller is set up as a Serial Peripheral Interface (SPI) master, while the RFID chip functions as an SPI slave in this design [61] [34]. This configuration enables efficient data transfer from the microcontroller to the RFID chip for storage or further processing. The microcontroller writes the digital magnetic field information to the EPC memory of the RFID chip through SPI. The detail of microcontroller configuration is presented in Appendix A. The EPC memory is the first writable memory within the RFID chip where data can be stored and retrieved. By storing the magnetic field data in the EPC memory, it becomes an integral part of the RFID tag and can be accessed and read by the RFID reader.

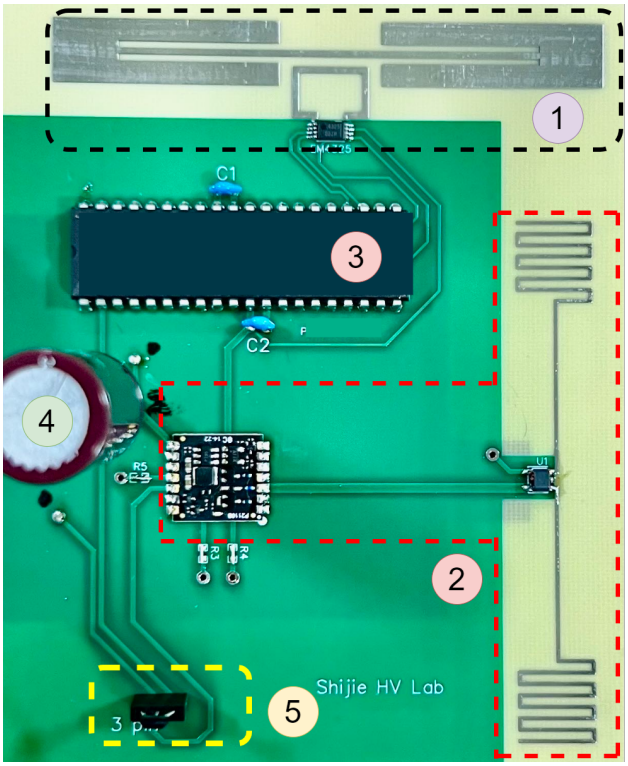

Fig. 6.1: Top view of the fabricated sensor (1.RFID tag 2. Power harvesting section 3. Microcontroller 4.Supercapacitor 5. Hall effect sensor).

6.2 Evaluation of Hall Effect Sensor

As discussed in Chapter 4, a Hall effect sensor is selected for the implementation of the RFID-based magnetic field sensor due to its ability to provide reliable and precise magnetic field measurements. Before fabricating the complete RFID tag, the Hall effect sensor is tested in a controlled setup to verify its performance and ensure it meets the required sensitivity and accuracy for overhead HVdc transmission line monitoring and current measurement applications.

The setup is shown in Fig. 6.2, and consists of a dc source and a 6 m transmission line conductor used for HVdc transmission networks. The dc source is capable of supplying a current of up to 1.2 kA. Detailed specifications of the source are attached in Appendix C. The HVdc conductor used is the same type employed in the HVdc transmission system by Manitoba Hydro. It has a diameter of 40 mm and consists of 50 strands of single conductors. The conductor is held above ground using 7 insulators. The Hall effect sensor is located 2.5 cm away from the conductor.

In this testing setup, the sensor's output is measured in response to a range of magnetic fields. The sensor is connected to a breadboard for power supply and ground connection where the analog output voltage corresponding to different magnetic field intensities is measured using a multimeter.

Based on Ampere's law, the magnetic field at the location of the Hall effect sensor, positioned 2.5 cm from the conductor's surface—ranges from 0 to 5.448 mT. As illustrated in Fig. 6.3, the results agree with the theoretical magnetic field values calculated using Ampere's law as the current is varied from 0 to 1.2 kA. The maximum observed deviation from the theoretical values is 2.7 %, indicating good agreement. Additionally, an experiment was conducted with a constant current while varying the distance between the Hall effect

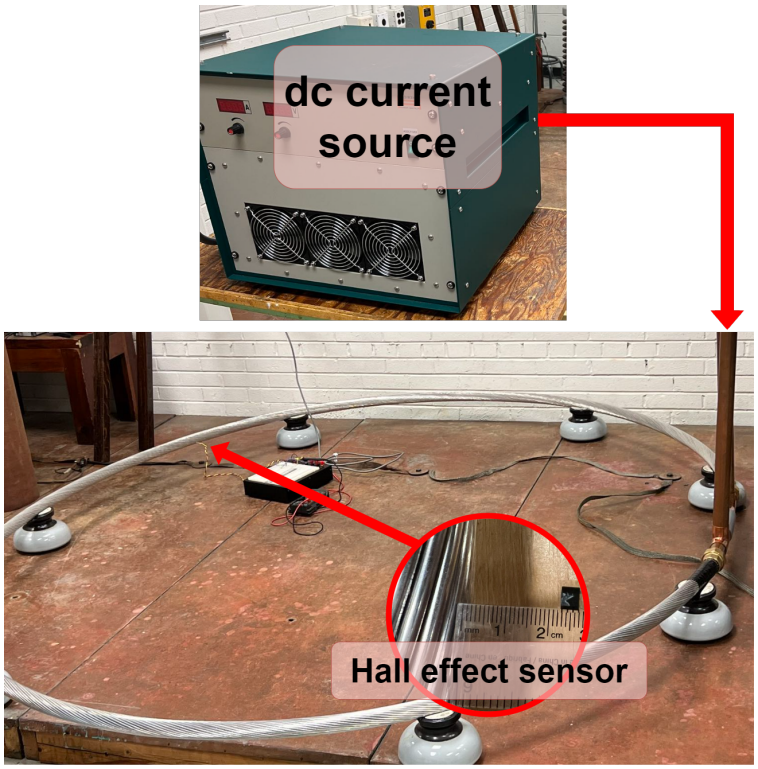

Fig. 6.2: Experiment setup for testing Hall effect sensor around HVdc conductor with a dc current source.

sensor and the conductor. The results, displayed in Fig. 6.4, also show agreement with the theoretical predictions, with a maximum deviation of 4.3 %. This consistency confirms the accuracy of the Hall effect sensor's response to changes in magnetic flux density with both current and distance, validating its use in field measurements based on Ampere's law.

These preliminary tests help calibrate the sensor, ensuring that it will function as expected when integrated into the RFID tag for magnetic field monitoring. The following sections will discuss the test setup and the result for the fabricated RFID based magnetic field sensor.

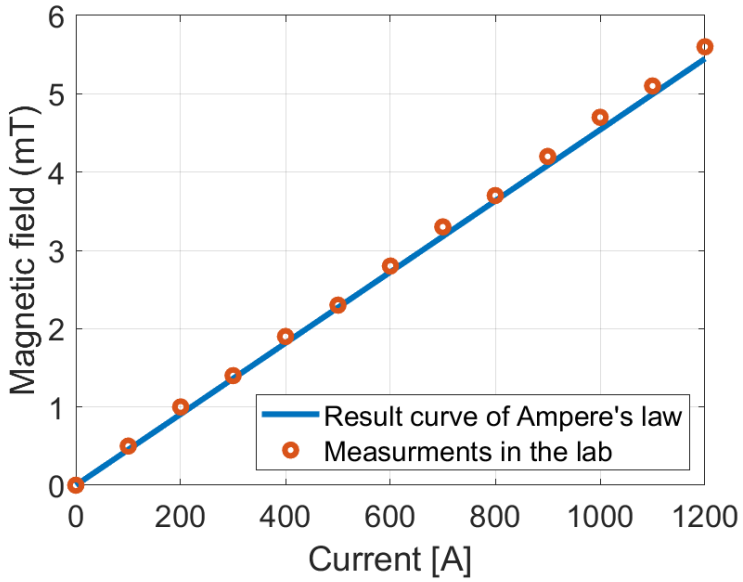

Fig. 6.3: Magnetic field measured around HVdc conductor by the Hall effect sensor with varying current.

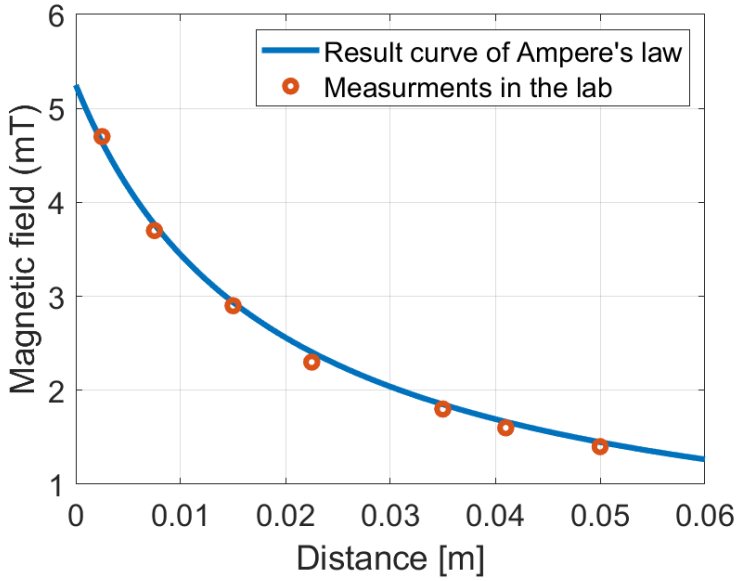

Fig. 6.4: Magnetic field measured around HVdc conductor by the Hall effect sensor with varying distance between the Hall effect sensor and HVdc conductor.

6.3 Evaluation of the RFID Magnetic Field Sensor

In this part of the experiment, the fabricated sensor is tested in the High Voltage Lab at the University of Manitoba. The tests focus on evaluating the sensor's performance by simulating the same conditions found in a HVdc transmission systems. Two distances (d) between the tag and the RFID reader (70 cm and 1 m) and two distances between the Hall effect sensor and the HVdc conductor is tested (0.5 cm and 3 cm) were tested. The test setup is shown in Fig. 6.5 and 6.6, from the top view and side view, respectively. The set up consists of a dc source that is capable of generating a current from $0 - 1200$ A. The source is connected to an HVdc conductor, which is the same as that employed in HVdc transmission lines in Manitoba. The HVdc conductor has a diameter of 4 cm and the loop made by the conductor has a diameter of 2 m. The sensing system is placed beside the conductor. The distance between the Hall effect sensor and the conductor, as shown in the figure, is 3 cm. The distance between the RFID based magnetic field sensor and the RFID reader is 1 m. The distance between the sensing system and the RFID reader does not affect the accuracy of magnetic field measurements, but only influences the charging time of the system. As discussed in Section 5.2, the charge time between each measurement is 5 s for a 70 cm reader-tag distance. When the reader-tag distance is increased to 1 m, the charge time between each measurement increased to 14 s. Additionally, an oscilloscope is used to monitor the capacitor voltage. During the time the voltage drop from maximum to threshold value, the measurements are performed. The time of the voltage change is 60 ms, and all commands will be executed during this time that include reading Hall effect sensor voltage and write the measurements to the RFID tag. The dc source used to generate the dc current in this experiment contains many internal switching circuits. The source itself generates significant electromagnetic interference during the charging process of the supercapacitor.

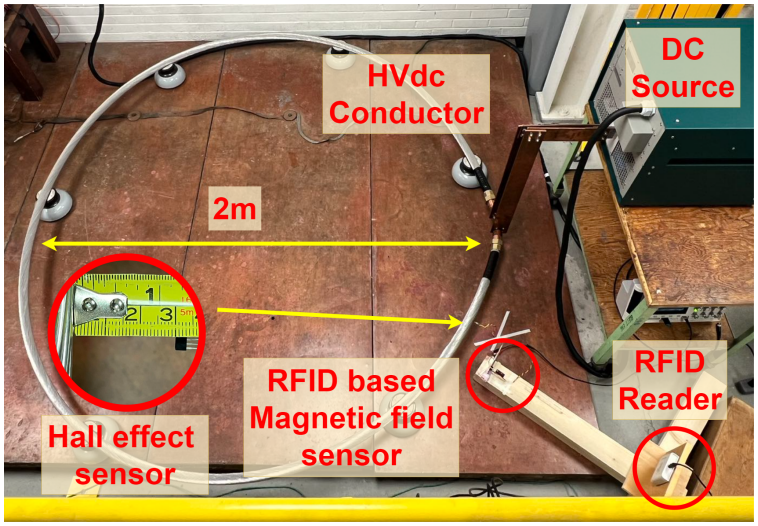

Fig. 6.5: Experiment setup for the measurement of magnetic flux density generated by a dc current flowing through a HVdc conductor (Top view).

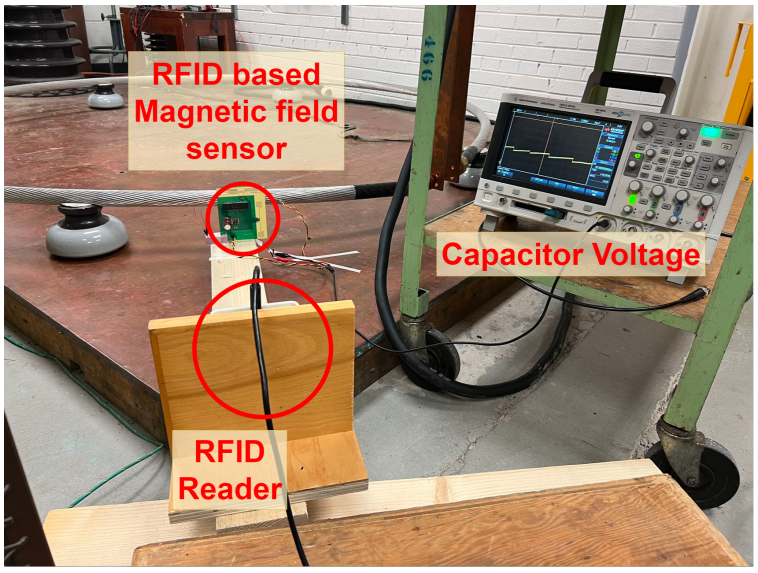

Fig. 6.6: Experiment setup for the measurement of magnetic flux density generated by a dc current flowing through a HVdc conductor (Side view).

6.3.1 Results and Discussions

The results of the measurements done in the laboratory are compared with a COMSOL simulation to validate the accuracy of the fabricated sensor. Table 6.1 shows the magnetic flux density simulated using COMSOL Multiphysics. The geometry set up in COMSOL is exactly the same as the setup, and the current is varied from 100 A to 1200 A.

Table 6.1: Simulated magnetic field for the setup.

I (A)	Magnetic flux density(mT) $d = 3\,cm$	Magnetic flux density (mT) $d = 0.5\,cm$
100	0.397	0.814
200	0.794	1.6287
300	1.1904	2.443
400	1.5872	3.2574
500	1.9839	4.0717
600	2.3807	4.8861
700	2.7775	5.7004
800	3.1743	6.5148
900	3.5711	7.3291
1000	3.9679	8.1435
1100	4.3647	8.9578
1200	4.7615	9.7722

The Hall effect sensor used to measure the magnetic field is DRV5055/A2. According to its datasheet, when the supply voltage is 3.3 V, the sensitivity is 30 mV/mT. The sensitivity obtained using the measured data in Fig. 6.7 can be calculated by

$$\text{Sensitivity} = \frac{\Delta\text{Voltage}}{\Delta\text{Magnetic flux density}} = \frac{1.763\ V - 1.634\ V}{4.76\ mT - 0\ mT} = 27.1\ \frac{mV}{mT} \tag{6.1}$$

which is close to the datasheet.

The first experiment was done with a 1 m reader-tag distance and a 3 cm sensor-conductor distance. The measurements and simulated magnetic flux density is shown in

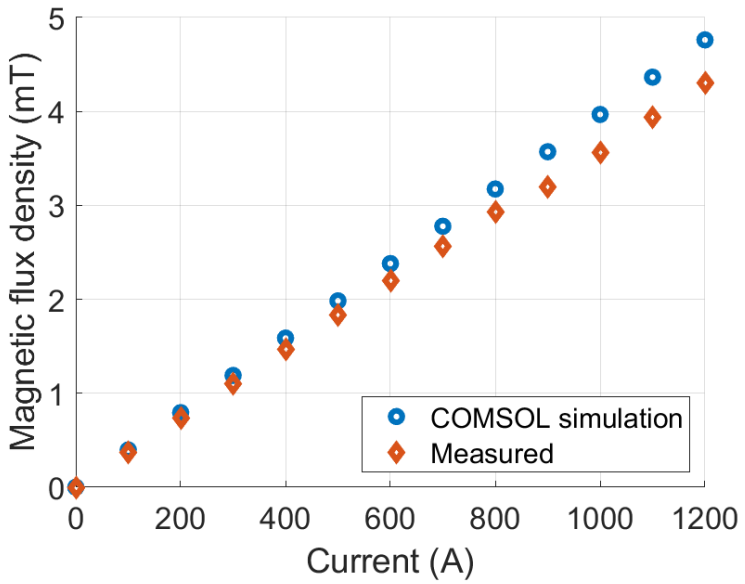

Fig. 6.7: Magnetic flux density measurement for HVdc conductor setup with $d = 3cm$ sensor-conductor distance. The measured values are compared with those simulated using COMSOL. The correlation coefficient of the measured magnetic field result is 0.9994 and the calibration factor calculated is 0.0036 mT/A.

Fig. 6.7. The RSS measured by the reader is −53 dBm, and the chargetime between measurements is 14 s. The correlation coefficient of the measured magnetic field result is 0.9994 which means that the sensor has a near perfect linear relationship between the magnetic field and current. The largest deviation between simulation and measurements is 10%.

The second experiment was done with a 1 m reader-tag distance and a 0.5 cm sensor-conductor distance. The measurements and simulated magnetic flux density is shown in Fig. 6.8. The RSS measured by the reader is −53 dBm, and the chargetime between measurements is 14 s. The correlation coefficient of the measured magnetic field result is 0.9998 which means that the sensor has a near perfect linear relationship between the magnetic field and current. The largest deviation between simulation and measurements is 7.3%. For both cases, the resolution of the magnetic field measurement is around 90 A.

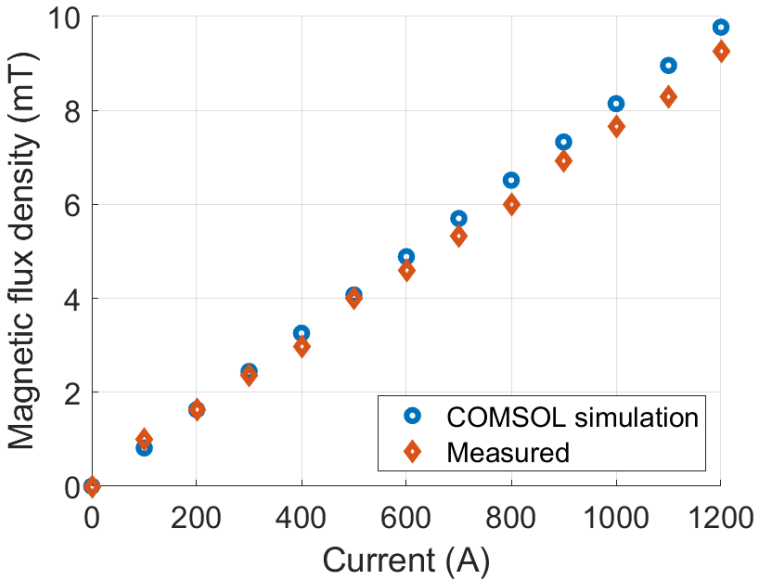

Fig. 6.8: Magnetic flux density measurement for HVdc conductor setup with $d = 0.5cm$ sensor-conductor distance. The measured values are compared with those Simulated using COMSOL. The correlation coefficient of the measured magnetic field result is 0.9998 and the calibration factor calculated is 0.0074 mT/A.

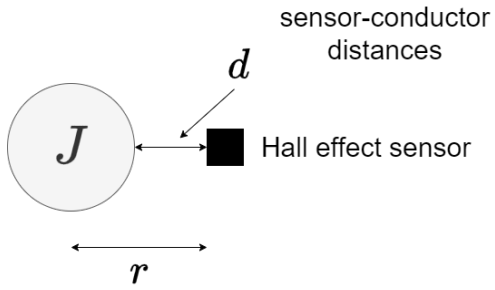

Fig. 6.9: Diagram demonstration of the distance between the Hall effect sensor and the conductor and the distance used in Ampere's law.

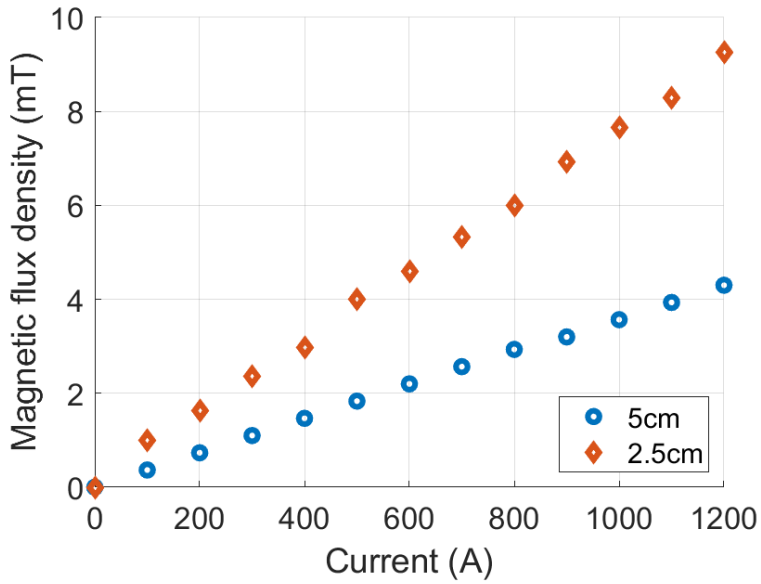

Fig. 6.10: Magnetic flux density measurement for HVdc conductor setup with $r = 2.5$ cm cm and $r = 5$ cm sensor-conductor distance.

After verifying the reliability of the measured magnetic field by the sensor, the two sets of result with different sensor-conductor distances are compared. Ampere's law states that the magnetic flux density around a infinite current carrying wire can be evaluated as

$$B = \frac{\mu_0 I}{2\pi r} \tag{6.2}$$

where μ_0 is $4\pi \times 10^{-7}$, r is the distance plus the radius of the conductor as shown in Fig. 6.9. The value of r is 2.5 and 5 cm for 0.5 and 3 cm sensor-conductor distance, respectively. By changing the sensor-conductor distance from 0.5 to 3 cm, r in Ampere's law is doubled. The calculated magnetic flux density should also double. Each measured magnetic field in the 0.5 cm case is around twice of the corresponding number in the 3 cm set which agrees with Ampere's law.

One of the most significant sources of error in this setup is the issue of electromagnetic interference caused by the current source. As shown in Fig. 6.11, the noise level measured across the capacitor is much higher when the source is ON. This interference is caused by the internal switching circuits within the current source, which generate high-frequency noise that couples with the measurement system. The noise from the environment might be a reason that causes the deviation between measurements and simulation.

6.4 Summary

In this chapter, the dc current setup for testing the Hall effect sensor and the fabricated sensor is presented. The first test validates the capability of using a Hall effect sensor to measure the magnetic flux density generated by dc current passing through an HVdc conductor. The second test evaluates the performance of the fabricated sensor. The sensor is tested at different sensor-conductor distances and reader-sensor distances. The results are compared with simulated results from a COMSOL Multiphysics simulation. The sensor demonstrates good performance in measuring the magnetic field around HVdc transmission lines, with a sensitivity of 27.1 mV/mT and a minimum current resolution of 90 A.

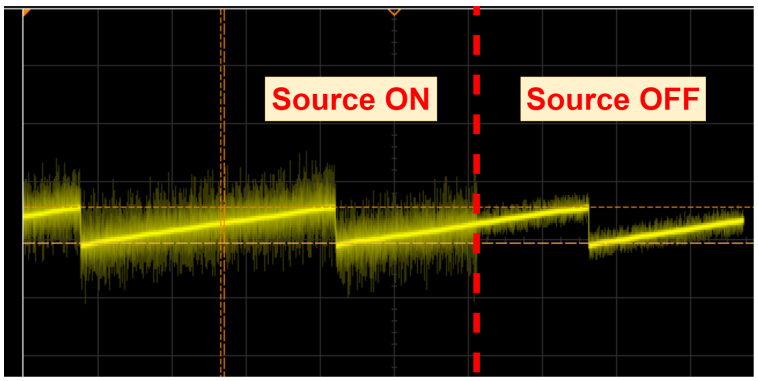

Fig. 6.11: Capacitor voltage measured using an oscilloscope showing the noise when the dc source is ON and OFF.

Chapter 7

Concluding Remarks

7.1 Conclusions

In this thesis, a UHF RFID system for measuring the dc magnetic field on HVdc transmission lines was designed, fabricated, and tested. The UHF RFID system design includes two antenna designs, microcontroller interfacing, and integration of an RF power harvester and a supercapacitor with a Hall effect sensor. Both the RFID antenna and the RF power harvester antenna were designed using Ansys HFSS to calculate the antenna impedance and ensure proper matching with the RFIC and the power harvester. These antennas were fabricated and tested using the half-antenna test method to measure their actual antenna impedance. Both antennas' impedances are close to the HFSS-simulated antenna impedances. Additionally, the gain of the power harvester antenna was measured using a relative antenna gain test, and the results indicate that the fabricated antenna has a gain of approximately 1 dBi. A commercial RFID reader was tested to verify its RF power output, reading range, and the received signal strength. The measured power spectrum agrees with the reader's frequency

and power level specifications. An experiment was conducted to test two different magnetic field sensors. A solenoid was used to generate a magnetic field equivalent to that of HVdc transmission lines. The Hall effect sensor showed good performance with a wider linear dynamic range and high sensitivity. The Hall effect sensor was chosen for the implementation of the RFID-based magnetic field sensor. A follow-up experiment was conducted using the Hall effect sensor and an HVDC conductor to verify its capability for actual HVDC magnetic field measurement. The results show that the Hall effect sensor is capable of measuring the magnetic field. The interfacing between the RFIC and a commercial microcontroller is described and discussed in Appendix A. The interfacing method used in this thesis is Serial Peripheral Interface (SPI). The RFIC chip is configured as an SPI slave to receive the measured magnetic field data and store it in the EPC memory of the RFIC. The RF power harvester implemented in this thesis, P2110B, is tested with the designed power harvester antenna. Measurements are taken only during the discharge time of the supercapacitor, which is controlled by the power management circuit integrated into the power harvester. The on-time for the entire circuit is 60 ms, and the magnetic field is captured and written to the RFIC during this on-time.

After all design validation tests, the fabricated RFID based magnetic field sensor was tested in the High Voltage Lab at the University of Manitoba. The sensor was evaluated at different sensor-conductor distances and reader-sensor distances. The sensor performed perfectly at a distance of 1 m, with an RSS measurement of -53 dBm, which is higher than the minimum detectable signal of -66 dBm. A sensitivity of 27.1 mV/mT and a minimum current resolution of 90 A were obtained. The sensitivity matches the specifications in the Hall effect sensor datasheet. All results were compared with COMSOL Multiphysics simulations, with the largest deviation being 10%. Overall, the fabricated sensor meets the design

objectives set at the beginning of this thesis. However, some future work can be done to improve the performance of the RFID-based magnetic field sensor.

7.2 Future Work

In this thesis, a UHF RFID System for measuring dc magnetic field on HVdc Transmission lines was introduced. The UHF RFID sensing system were designed according to the EPC Radio-Frequency Identity Generation-2 UHF RFID Standard. The sensing system can be extended, and more sensors can be integrated to improve the overall performance of the sensing system.

In this section, further studies and possible extended applications are suggested.

- Optimizing tag design to improve sensitivity and read range is important, as read range is a limiting factor for applications in power system asset monitoring. Incorporating a high-gain antenna with a high-efficiency RFIC should be explored.

- A magnetic field sensor that has better sensitivity can be employed to perform more precise measurements and decrease the current resolution for HVdc transmission line monitoring and current measurements.

- An electric field sensor can be added to the system to to perform magnetic field and electric field measurement at the same time.

- A hybrid power harvester that acquires energy from various ambient sources can enhance system functionality. In a typical RFID system, the transmitter is limited to an output power of no more than 36 dBm, which restricts the power budget and limits

the number of components on the same tag. Incorporating multiple power harvesters that draw from diverse ambient sources can expand the system's overall functionality.

- A deep learning algorithm can be integrated with the UHF RFID sensing system to perform diagnosis or prognosis of the behavior of power system assets.

- Standardization of RFID technology usage in power system monitoring is essential. Modern control systems for power asset management and control involve numerous wireless devices. To ensure effective monitoring of power system assets, it is crucial that future UHF RFID implementations avoid interference with other devices.

References

[1] D. V. Hertem, O. Gomis-Bellmunt, and J. Liang, *HVDC grids : for offshore and supergrid future*, ser. IEEE press series on power engineering. Hoboken, New Jersey: Wiley, 2016.

[2] D. Jovcic and K. Ahmed, "Introduction to line-commutated HVDC," in *High Voltage Direct Current Transmission*. Aberdeen, UK: Wiley, 2019, pp. 4–7.

[3] A. H. Khawaja, Q. Huang, and Z. H. Khan, "Monitoring of overhead transmission lines: A review from the perspective of contactless technologies," *Sensing and imaging*, vol. 18, no. 1, pp. 1–18, 2017.

[4] G. D'Antona, L. Di Rienzo, R. Ottoboni, and A. Manara, "Processing magnetic sensor array data for ac current measurement in multiconductor systems," *IEEE Transactions on Instrumentation and Measurement*, vol. 50, no. 5, pp. 1289–1295, 2001.

[5] Z. Zhang and L. Di Rienzo, "Optimization of magnetic sensor arrays for current measurement based on swarm intelligence and d-optimality," *Compel*, vol. 28, no. 5, pp. 1179–1190, 2009.

[6] P. Ripka, "Electric current sensors: a review," *Measurement science & technology*, vol. 21, no. 11, pp. 112 001–23, 2010.

[7] M. Zhu and K. Xu, "A calibrating device for large direct current instruments up to 320 kiloampere-turns," *IEEE Transactions on Instrumentation and Measurement*, vol. 47, no. 3, pp. 711–714, 1998.

[8] L. Callegaro, C. Cassiago, and E. Gasparotto, "On the calibration of direct-current current transformers (DCCT)," *IEEE Transactions on Instrumentation and Measurement*, vol. 64, no. 3, pp. 723–727, 2015.

[9] H. Rahmani, D. Shetty, M. Wagih, Y. Ghasempour, V. Palazzi, N. B. Carvalho, R. Correia, A. Costanzo, D. Vital, F. Alimenti, J. Kettle, D. Masotti, P. Mezzanotte, L. Roselli, and J. Grosinger, "Next-generation iot devices: Sustainable eco-friendly manufacturing,

energy harvesting, and wireless connectivity," *IEEE Journal of Microwaves*, vol. 3, no. 1, pp. 237–255, Jan 2023.

[10] R. Colella, L. Tarricone, and L. Catarinucci, "Spartacus: Self-powered augmented RFID tag for autonomous computing and ubiquitous sensing," *IEEE Transactions on Antennas and Propagation*, vol. 63, no. 5, pp. 2272–2281, 2015.

[11] *EPC Radio-Frequency Identity Generation-2 UHF RFID Standard: Specification for RFID Air Interface Protocol for Communications at 860 MHz – 930 MHz*, GS1 US, 1 2024.

[12] S. Fu, G. E. Bridges, and B. Kordi, "Application of radio frequency identification (RFID) in power systems monitoring," in *CIGRE Canada*, Winnipeg, Canada, 28-31 October 2024.

[13] S. Fu, G. Bridges, and B. Kordi, "Magnetic field monitoring on HVdc transmission lines using a UHF-RFID tag," in *2024 Photonics and Electromagnetics Research Symposium (PIERS 2024)*, Chengdu, China, 21-25 April 2024.

[14] J. Arrillaga, *High voltage direct current transmission*, 2nd ed., ser. IEE power and energy series ; 29. London: Institution of Electrical Engineers, 1998.

[15] K. Zhu, W. K. Lee, and P. W. T. Pong, "Non-contact electric-coupling-based and magnetic-field-sensing-assisted technique for monitoring voltage of overhead power transmission lines," in *2015 IEEE SENSORS*, 2015, pp. 1–4.

[16] X. Sun, Q. Huang, Y. Hou, L. Jiang, and P. W. T. Pong, "Noncontact operation-state monitoring technology based on magnetic-field sensing for overhead high-voltage transmission lines," *IEEE Transactions on Power Delivery*, vol. 28, no. 4, pp. 2145–2153, 2013.

[17] Q. Huang, W. Zhen, and P. W. T. Pong, "A novel approach for fault location of overhead transmission line with noncontact magnetic-field measurement," *IEEE Transactions on Power Delivery*, vol. 27, no. 3, pp. 1186–1195, 2012.

[18] M. Paranjape, L. Ristic, and I. Filanovsky, "A 3-d vertical hall magnetic field sensor in cmos technology," in *Transducers '91: 1991 International Conference on Solid-State Sensors and Actuators. Digest of Technical Papers*, 1991, pp. 1081–1084.

[19] J. R. Brauer, *Hall Effect and Magnetoresistive Sensors*. Wiley, 2014, pp. 175–199.

[20] E. Ramsden, "Hall-effect physics," in *Hall-Effect Sensors*, 2nd ed. United States: Elsevier, 2006, pp. 1–1.

[21] *1- and 2-Axis Magnetic Sensors HMC1001/1002/1021/1022*, Honeywell, 4 2019.

[22] F. Shi, X. Bai, F. Wang, F. Pang, S. Pu, and X. Zeng, "All-fiber magnetic field sensor based on hollow optical fiber and magnetic fluid," *IEEE Sensors Journal*, vol. 17, no. 3, pp. 619–622, 2017.

[23] R. Lv, Y. Zhao, D. Wang, and Q. Wang, "Magnetic fluid-filled optical fiber Fabry–Pérot sensor for magnetic field measurement," *IEEE Photonics Technology Letters*, vol. 26, no. 3, pp. 217–219, Feb 2014.

[24] Z. Lu, S. Chen, and J. Chen, "A study of the optical measurements of high-voltage current using magnetic fluid films," *Guangxué xuébào*, vol. 27, no. 6, pp. 1049–1051, 2007.

[25] B. Li, O. Yassine, and J. Kosel, "Integrated passive and wireless sensor for magnetic fields, temperature and humidity," in *IEEE SENSORS*, 2013, pp. 1–4.

[26] ——, "A surface acoustic wave passive and wireless sensor for magnetic fields, temperature, and humidity," *IEEE Sensors Journal*, vol. 15, no. 1, pp. 453–462, 2015.

[27] K. Chen, Y. Zhu, Z. Liu, and D. Xue, "State of the art in crystallization of linbo3 and their applications," *Molecules*, vol. 26, no. 22, 2021. [Online]. Available: https://www.mdpi.com/1420-3049/26/22/7044

[28] J. V. de Almeida, X. Gu, and K. Wu, "SWIPT base stations for battery-free, wirelessly powered IoT networks: A review on architectures, circuits and technologies," *IEEE Microwave Magazine*, vol. 25, no. 6, pp. 22–40, 2024.

[29] N. Raza, V. Bradshaw, and M. Hague, "Applications of RFID technology," in *IEE Colloquium on RFID Technology (Ref. No. 1999/123)*, 1999, pp. 1/1–1/5.

[30] N. C. Karmakar, *Introduction to RFID Systems*. Wiley, 2010, pp. 13–56.

[31] C. Yang, J. He, and Y. Kun, "RFID Tag Anti-Collision Protocols," in *Advanced RFID Systems, Security, and Applications*. Hersey: Igi Global, 2013, pp. 133–154.

[32] M. Bolic, D. Simplot-Ryl, I. Stojmenovic, M. Bolic, I. Stojmenovic, and D. Simplot-Ryl, *RFID Systems: Research Trends and Challenges*, 1st ed. Newark: Wiley, 2010.

[33] K. Finkenzeller, *RFID handbook fundamentals and applications in contactless smart cards and identification*, 2nd ed. Chichester, England ;: Wiley, 2003.

[34] *EM4325 18000-63 Type C (Gen2) and 18000-63 Type C / 18000-64 Type D (Gen2/TOTAL) RFID IC*, em microelectronics, 2 2023, version 9.2.

[35] A. P. Sample, D. J. Yeager, P. S. Powledge, A. V. Mamishev, and J. R. Smith, "Design of an RFID-Based battery-free programmable sensing platform," *IEEE Transactions on Instrumentation and Measurement*, vol. 57, no. 11, pp. 2608–2615, 2008.

[36] C. Occhiuzzi, S. Parrella, F. Camera, S. Nappi, and G. Marrocco, "RFID-Based dual-chip epidermal sensing platform for human skin monitoring," *IEEE Sensors Journal*, vol. 21, no. 4, pp. 5359–5367, 2021.

[37] A. E. Abdulhadi and R. Abhari, "Multiport UHF RFID-Tag antenna for enhanced energy harvesting of self-powered wireless sensors," *IEEE Transactions on Industrial Informatics*, vol. 12, no. 2, pp. 801–808, 2016.

[38] Z. Li, G. Li, G. Wen, R. Xu, J. Li, Y. Huang, H. Sun, P. Wu, D. Inserra, and F. Xie, "Intermittent magnetic field monitoring system based on passive RFID sensor tags," *IEEE Sensors Journal*, vol. 22, no. 1, pp. 819–831, 2022.

[39] N. Sakai, K. Noguchi, and K. Itoh, "A 5.8-GHz band highly efficient 1-W rectenna with short-stub-connected high-impedance dipole antenna," *IEEE Transactions on Microwave Theory and Techniques*, vol. 69, no. 7, pp. 3558–3566, 2021.

[40] Y. Muramoto, N. Sakai, and K. Itoh, "A 920 mhz band rectenna with the impedance transfomed small loop antenna (IT-SLA)," in *Wireless Power Week (WPW)*, 2022, pp. 400–403.

[41] T. Mitani, S. Kawashima, and T. Nishimura, "Analysis of voltage doubler behavior of 2.45-GHz voltage doubler-type rectenna," *IEEE Transactions on Microwave Theory and Techniques*, vol. 65, no. 4, pp. 1051–1057, 2017.

[42] W. Jian, Z. Mengzhao, Z. Wenbing, G. Zhaoliang, W. Xuelei, and Z. Qingdong, "The self-powered RFID sensor system for power transformer condition monitoring," in *2021 IEEE 4th Advanced Information Management, Communicates, Electronic and Automation Control Conference (IMCEC)*, vol. 4, 2021, pp. 613–617.

[43] T. Wang, Y. He, Q. Luo, F. Deng, and C. Zhang, "Self-powered RFID sensor tag for fault diagnosis and prognosis of transformer winding," *IEEE Sensors Journal*, vol. 17, no. 19, pp. 6418–6430, 2017.

[44] C. Zhang, Y. He, S. Jiang, T. Wang, L. Yuan, and B. Li, "Transformer fault diagnosis method based on self-powered RFID sensor tag, DBN, and MKSVM," *IEEE Sensors Journal*, vol. 19, no. 18, pp. 8202–8214, 2019.

[45] A. Amirkabiri, D. Idoko, B. Kordi, and G. E. Bridges, "Chipless RFID sensor for measuring time-varying electric fields using a contactless air-filled substrate-integrated waveguide resonator," *Sensors*, vol. 24, no. 15, 2024. [Online]. Available: https://www.mdpi.com/1424-8220/24/15/4928

[46] Z. Yang, K. Y. See, M. F. Karim, and A. Weerasinghe, "Chipless RFID-based sensing system for partial discharge detection and identification," *IEEE Sensors Journal*, vol. 21, no. 2, pp. 2277–2285, 2021.

[47] N. C. Karmakar, "Chipless RFID sensor for high voltage condition monitoring," in *Advanced RFID Systems, Security, and Applications*. Hersey: IGI Global, 2012, pp. 304–333.

[48] S. M. Kayser Azam, M. Othman, T. A. Latef, H. A. Illias, A. K. M. Z. Hossain, and A. A. Ababneh, "Chipless RFID tag by V-shaped multi-resonator for partial discharge-affected equipment identification," in *Innovations in Power and Advanced Computing Technologies (i-PACT)*, 2023, pp. 1–5.

[49] H. Raihani, A. Benbassou, M. El Ghzaoui, and J. Belkadid, "Performance evaluation of a passive UHF RFID tag antenna using the embedded T-Match structure," in *International Conference on Wireless Technologies, Embedded and Intelligent Systems (WITS)*, 2017, pp. 1–6.

[50] N. Popović and P. Manojlović, "UHF RFID antenna: A printed dipol antenna with CPS matching circuit and inductively coupled feed," in *International Conference on Telecommunication in Modern Satellite, Cable, and Broadcasting Services*, 2009, pp. 445–448.

[51] H. Son and C. Pyo, "Design of RFID tag antennas using an inductively coupled feed," *Electronics letters*, vol. 41, no. 18, pp. 994–996, 2005.

[52] N. Popovic, "UHF RFID antenna: Printed dipole antenna with a CPS matching circuit and inductively coupled feed," *International Journal of Engineering Business Management*, vol. 4, no. 1, pp. 20–, 2012.

[53] L. Catarinucci, R. Colella, and L. Tarricone, "Enhanced UHF RFID sensor-tag," *IEEE Microwave and Wireless Components Letters*, vol. 23, no. 1, pp. 49–51, 2013.

[54] C. A. Balanis, *Antenna theory : analysis and design*, 4th ed., ser. New York Academy of Sciences. Hoboken, New Jersey: Wiley, 2016 - 2016.

[55] G. Marrocco, "The art of UHF RFID antenna design: impedance-matching and size-reduction techniques," *IEEE Antennas and Propagation Magazine*, vol. 50, no. 1, pp. 66–79, 2008.

[56] H. Ge, Y. Yao, J. Yu, X. Chen, and D. Valderas, "Straight-forward impedance measurement for balanced RFID tag antenna," *Electronics letters*, vol. 52, no. 3, pp. 181–182, 2016.

[57] R. Meys and F. Janssens, "Measuring the impedance of balanced antennas by an S-parameter method," *IEEE Antennas and Propagation Magazine*, vol. 40, no. 6, pp. 62–65, 1998.

[58] Y. Tikhov, Y. Kim, and Y.-H. Min, "Compact low cost antenna for passive RFID transponder," in *IEEE Antennas and Propagation Society International Symposium*, 2006, pp. 1015–1018.

[59] *DRV5055 Ratiometric Linear Hall Effect Sensor*, Texas instruments, 4 2021.

[60] *P2110B 915 MHz RF Powerharvester receiver*, powercast, 12 2016.

[61] *28/40/44-pin, Low-Power, High-Performance Microcontrollers PIC18F27/47Q10*, Microchip, 5 2024.

Appendix A

Serial Peripheral Interfacing (SPI)

Microcontroller is the most important part in the digital function block of the sensor tag design. In this design a Microchip ultra low power 10-bits microncontroller PIC18F47Q10 is used. The maximum current drawn is 4.4 mA with a 3.3V power supply. The PIC18F47Q10 microcontroller also includes an array of additional features that are suitable to the implementation of the RFID based magnetic field sensor. It operates at speeds up to 64 MHz and includes a range of peripherals such as multiple serial communication interfaces (USART, SPI, I2C). The clock speed can be modified by setting a specific register in the chip. The device also supports multiple timers, a 10-bit Analog-to-Digital Converter (ADC). This combination of features and flexibility makes the PIC18F47Q10 suitable for applications in implementing the RFID based magnetic field sensor.

To encode the measured magnetic field information. The ADC will be used to convert the voltage output from the Hall effect sensor. The ADC is configured to sample the analog input voltage at a 3.3V reference voltage. This means that the ADC only sample voltages between 0V and 3.3V, transferring them to corresponding 10-bit binary values within this

range. During each sampling period, the ADC compares the input voltage to the internal reference voltage to determine its approximate digital value. The resulting output is a 10-bit digital code, which provides a resolution of 1024 distinct values from $0 - 3.3$ V. This ensures that any small changes in the analog signal can be accurately captured. This digital code is then transmitted to the RFID chip.

To write the digital code to the EPC memory of the RFID chip, it is first converted to a hexadecimal format for compatibility with the RFID memory structure. Then the hexadecimal number is transmitted to the RFID chip over the SPI bus, with the RFID chip configured as an SPI slave device, allowing it to receive data directly from the controlling microcontroller. The EM4325 RFID chip receives these data and stores them in a designated memory location controlled by the microcontroller,ensuring that the measured magnetic field data is correctly logged in the EPC memory.

In SPI Slave mode, this device is configured to accept an SPI clock that operates independently of its internal processes. The SPI polarity and phase are configured through the SPI Control word. When the SPI Master clock (SCLK) operates, the maximum frequency is 2 MHz for battery assisted passive mode. The SPI Master needs to release the Chip Select (CS) line for at least 15 µs between commands. The device's maximum response time to an SPI command is 20 ms, and any response will start with a data value of '1'. The following example show in Fig. A.1 demonstrates how this device operates as an SPI Slave to communicate with an external SPI Master [34].

To verify the digital data coming out of the microcontroller is correct. A logic analyzer is used to visualize the digital signal. As shown in Figure A.2, the clock used for the SPI interface which should not be larger than 2 MHz is set to be 1.5 MHz [34]. The Master Output Slave Input (MOSI) bus is used to transmit three bytes: the command for enabling

writing function, the address where the data will be stored and the measured magnetic field data.

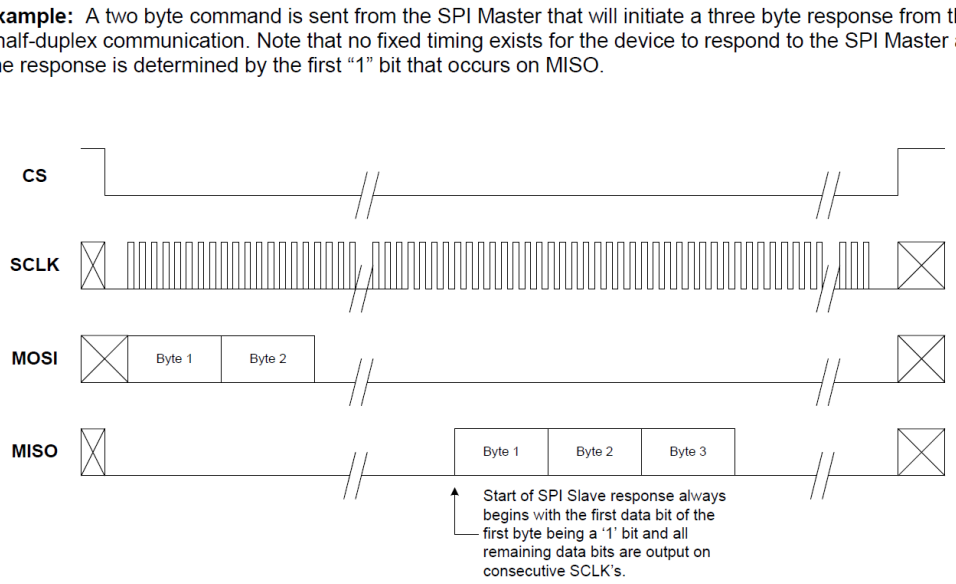

Fig. A.1: SPI slave example adopted from [34].

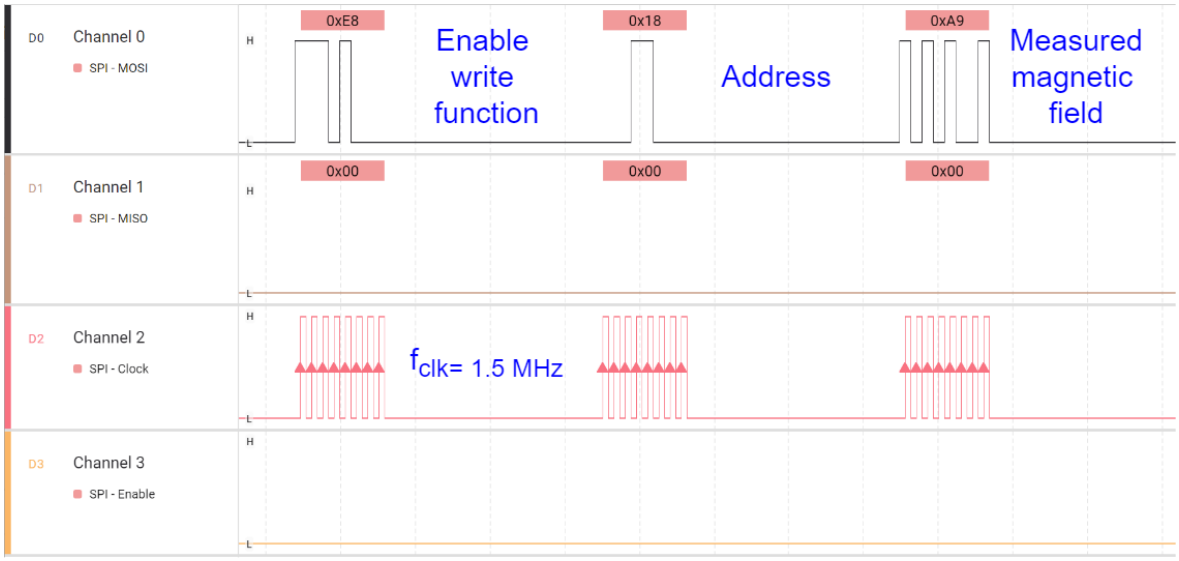

Fig. A.2: Digital signal going to the SPI slave measured with logic signal analyzer .

Appendix B

Specifications of RF Power Harvester P2110B

Parameter	Rating	Unit
RF Input Power	23	dBm
RF_{IN} to GND	0	V
D_{SET} to GND	6	V
RESET to GND	6	V
V_{CAP} to GND	2.3	V
V_{Out} to GND	6	V
Vout Current	100	mA
Operating Temperature Range	−40 to 85	°C
Storage Temperature Range	−40 to 140	°C

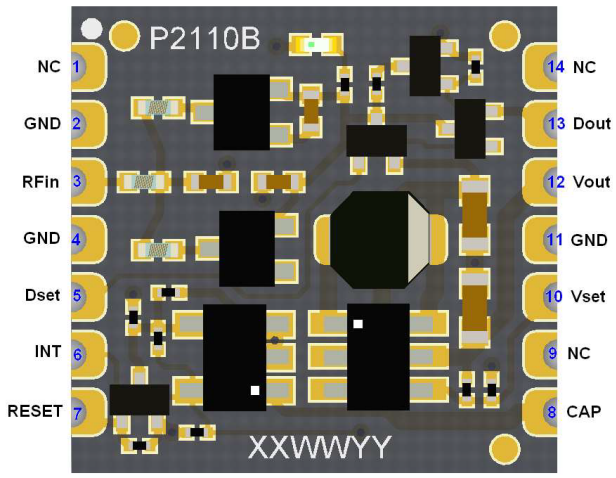

Fig. B.1: Pin configuration top view.

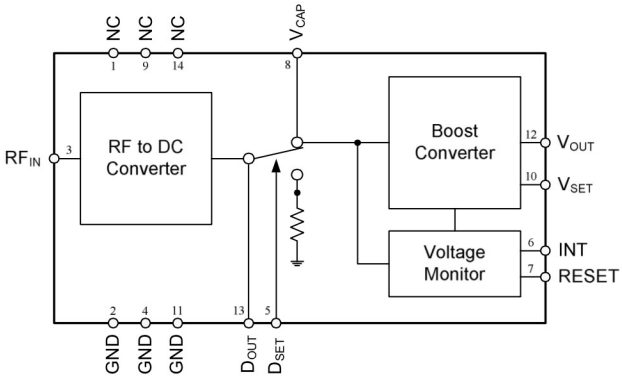

Fig. B.2: Functional block diagram of P2110B.

Table B.1: Pin functional descriptions.

Pin	Label	Function
1	NC	No Connection.
2	GND	RF Ground. Connect to analog ground plane.
3	RF_{IN}	RF Input. Connect to 50Ω antenna through a 50Ω transmission line. Add a DC block if antenna is a DC short.
4	GND	RF Ground. Connect to analog ground plane.
5	D_{SET}	Digital Input. Set to enable measurement of harvested power. If this function is not desired leave NC.
6	INT	Digital Output. Indicates that voltage is present at V_{out} .
7	RESET	Digital Input. Set to disable V_{our} . If this function is not desired leave NC.
8	V_{CAP}	Connect to an external capacitor for energy storage.
9	NC	No Connection.
10	V_{SET}	Output Voltage Adjustment. Sets the output voltage by connecting a resistor to V_{out} or GND. Leave NC for 3.3V.
11	GND	DC Ground. Connect to analog ground plane.
12	V_{OUT}	DC Output. Connect to external device. The output is preset to 3.3 V but can be adjusted with an external resistor.
13	D_{out}	Analog Output. Provides an analog voltage level corresponding to the harvested power.
14	NC	No Connection.

Appendix C

Specifications of DC Source

The description and technical specification of the dc source used for the dc current experiment is introduced in this section.

Description:

- **Switch mode (IGBT) bench case DC rectifier:**
  - < 3 % ripple through full output range for consistent process results.
  - High efficiency and power factor through the full output range
  - 100% duty cycle (rated for 100% output 24/7)
  - Ecoat primed, powder coat top coat metal enclosure for excellent corrosion resistance
  - DC output: copper bus bars out the rear of the enclosure
- **Cooling**
  - Air flow direction: intake in the front, exhaust in the back

  - Minimal cooling air required: variable speed, thermostatically controlled fans
  - Variable fans provide quiet operation
  - All sensitive electronics are sealed from the cooling air
  - Air is directed only to the heat sinks cooling the power components
  - All circuit boards are conformal coated for additional corrosion protection

- **Controls Interface:**
  - Digital DC voltmeter
  - Digital DC current meter
  - Nominal value setter DC voltage 0 - 100%
  - Nominal value setter DC current 0 - 100%
  - Fused rectifier On/Off toggle switch

- **Main Components:**
  - Fused power switch
  - EMC filter
  - Power semiconductors for power control and rectification
  - Electronics for constant current and voltage control

- **Protection Devices:**
  - Over-current protection
  - Short-circuit protection

Table C.1: Technical specification of the DC source.

Input Voltgae:	208V, 3Ph, 50-60Hz + GND
Input current:	18A
Power factor:	> 0.94
Rated DC voltage:	10 V
Rated DC current:	1200 A
Duty factor:	100%
Ripple voltage:	$< 3\%$ across full output range
Setting:	0 - 100% current and voltage
Control:	Constant current and voltage control
Control accuracy:	$< 1\%$ of rated output
Cooling:	Forced air-cooled
Ambient temperature:	Up to 95°F (35°C)
Site altitude:	Up to 3280 ft. above sea-level
Dimensions:	19.9 W x 21.6 D x 17.6 H inches
Weight:	175 lbs.
Enclosure rating:	NEMA 2 (IP11)

Fig. C.1: Photo of the DC source.

Appendix D

Schematic of The Fabricated Sensor

The printed circuit board (PCB) for this project was designed using EasyEDA, a user-friendly pcb design tool that provides library managements. After completing the design, the PCB was sent for fabrication to PCBWay, a professional PCB manufacturing company known for its high-quality production services, quick turnaround times, and global shipping.

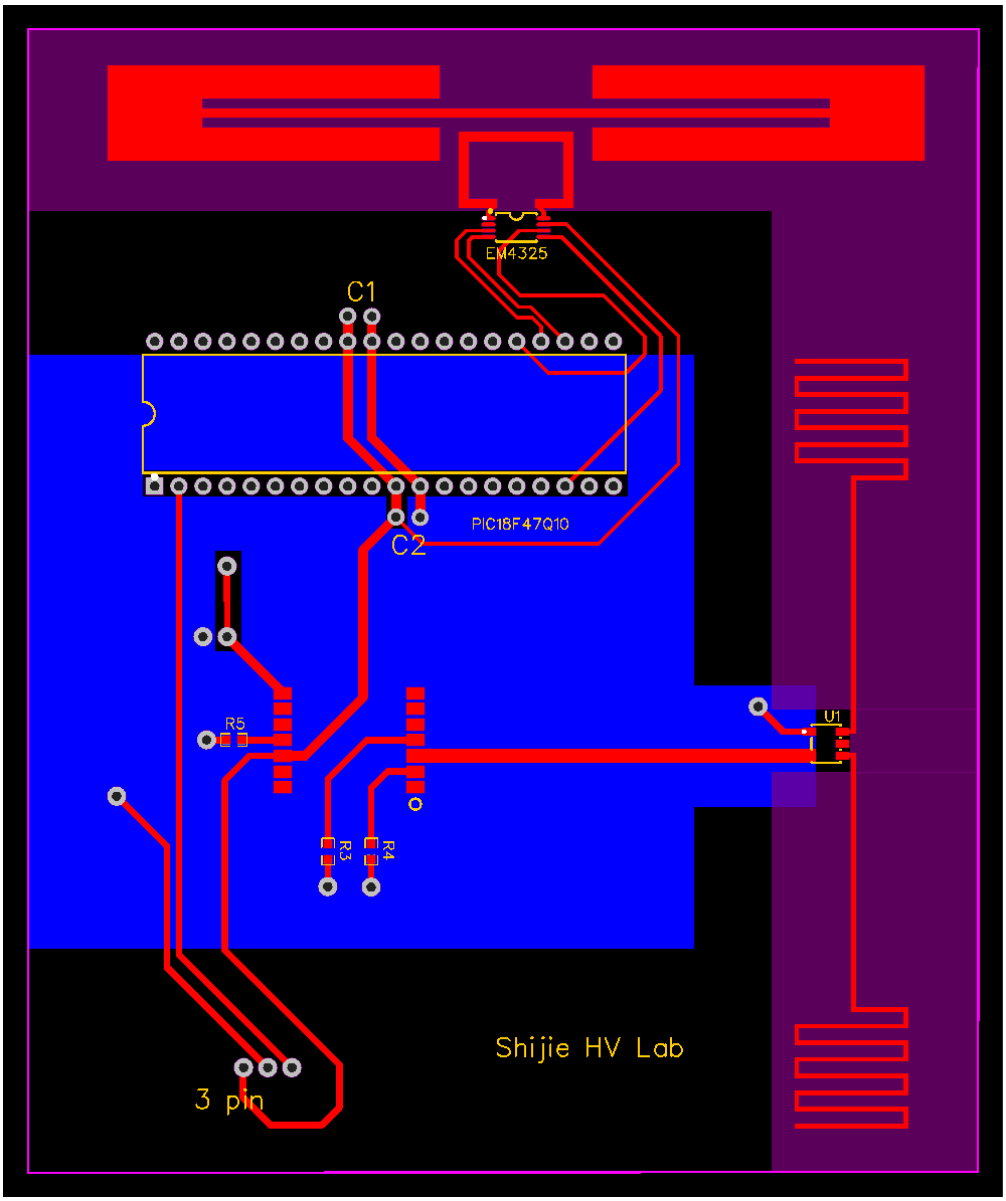

Fig. D.1: PCB layout.

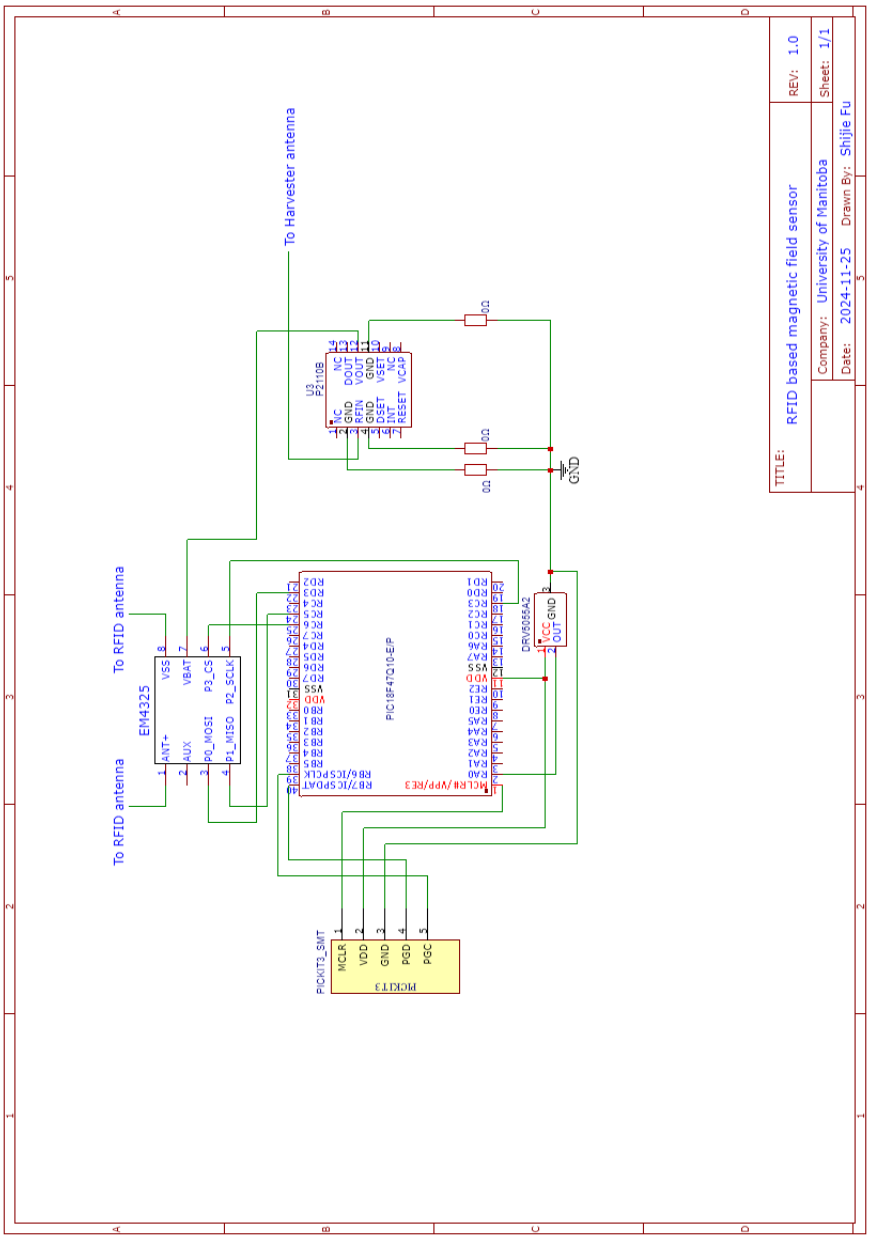

Fig. D.2: Schematic of the fabricated RFID based magnetic field Sensor.

Appendix E

RFID Reader - User Manual

This section shows the user manual on how to operate the RFID reader used in this thesis. Figure E.1 E.2 E.3 shows the setting window before reading starts. Figure E.4 shows the window when reading is in progress.

The displayed tag information can be modified for different parameters such as phase, frequency and ID etc. Most of the settings should be kept as default unless specific needs require changes, for example, the baud rate should be kept as 115200 all time during reading. Data export function is not recommended. The program will generate a .csv file but the information is the same as displayed on the screen, not all parameters will be exported.

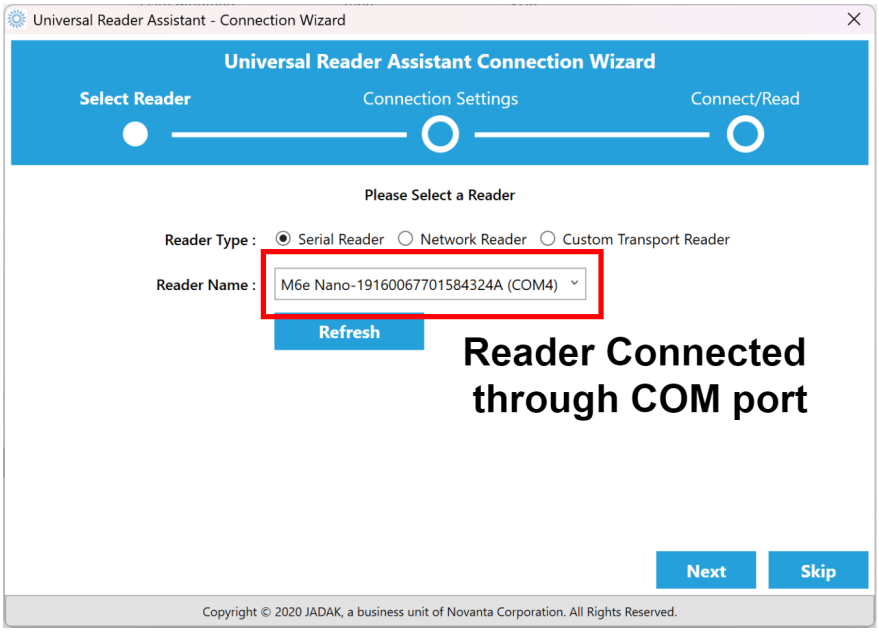

Fig. E.1: Screenshot showing reader connected through COM port.

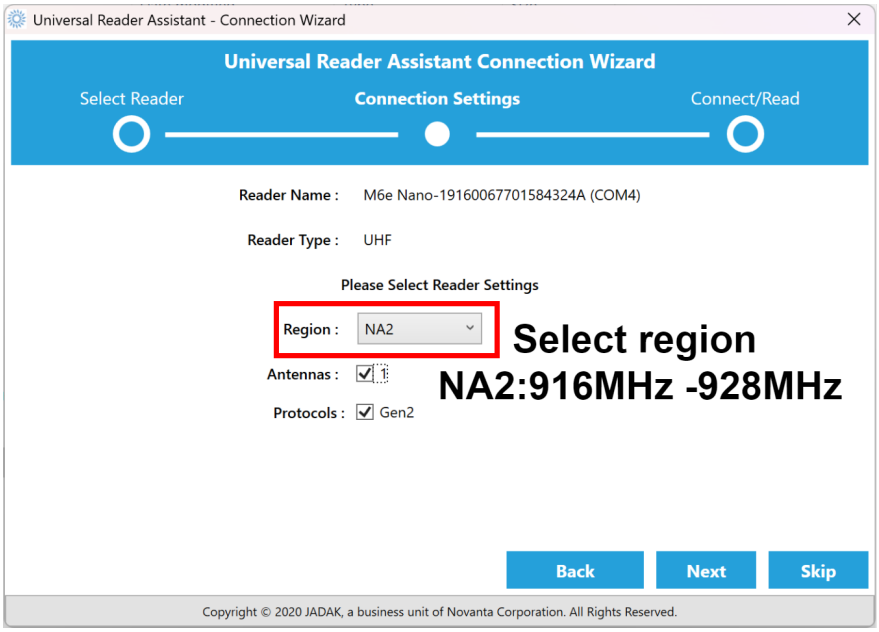

Fig. E.2: Screenshot showing the region and antenna selection.

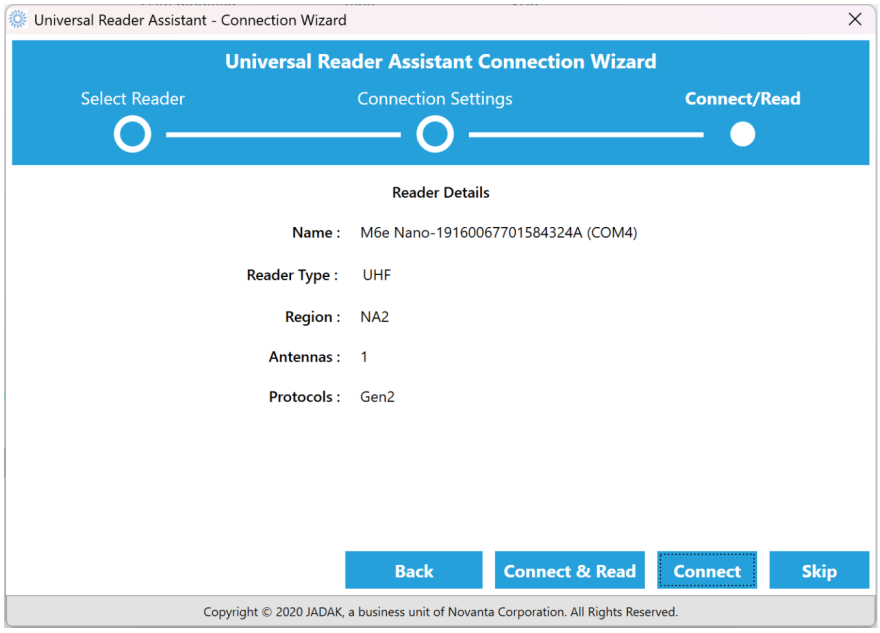

Fig. E.3: Screenshot showing reader details after all selections.

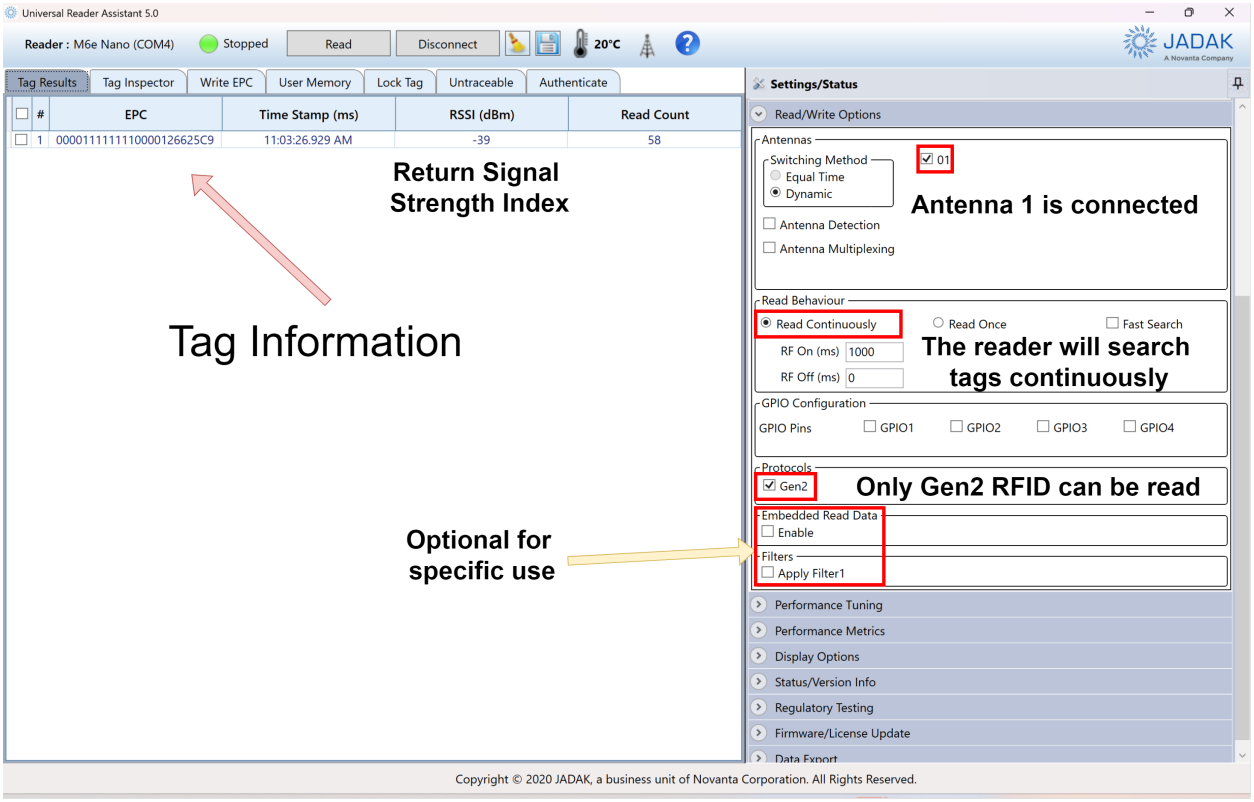

Fig. E.4: Screenshot showing the tag information and settings and status of the RFID reader.